GROSSITE-BEARING REFRACTORY INCLUSIONS FROM REDUCED CV CHONDRITES: MINERALOGICAL AND OXYGEN ISOTOPIC CONSTRAINTS ON THE PARENT BODY ALTERATION HISTORY

Jangmi Han[a,d,*], Kazuhide Nagashima[b], Changkun Park[c], Alexander N. Krot[b], and Lindsay P. Keller[d]

[a]Department of Earth and Atmospheric Sciences, University of Houston, Houston, TX 77204, USA

[b]Hawai'i Institute of Geophysics and Planetology, University of Hawai'i at Mānoa, Honolulu, HI 96822, USA

[c]Division of Glacier and Earth Sciences, Korea Polar Research Institute, 26 Songdomirae-ro, Yeonsu-gu, Incheon 21990, South Korea

[d]ARES, NASA Johnson Space Center, 2101 NASA Parkway, Houston, TX 77058, USA

*Corresponding author. Email address: Jangmi.han@nasa.gov.

Abstract

We report the results of coordinated mineralogical, microstructural, and oxygen isotopic analyses of grossite-bearing refractory inclusions from reduced CV (Vigarano type) chondrites to obtain a more complete picture of secondary parent body alteration processes and conditions. Grossite ($CaAl_4O_7$) occurs in cores of nodules in fine-grained Ca,Al-rich inclusions (CAIs) that likely represent aggregates of nebular condensates. In many occurrences, grossite has been partially replaced by hercynite [$(Fe,Mg,Zn)Al_2O_4$], which displays complex microstructures and compositions, and magnetite nanoparticles. The alteration of grossite was a crystallographically-controlled, fluid-driven process that occurred via partial dissolution of grossite and subsequent precipitation of hercynite and magnetite during short-lived and low-temperature metasomatic alteration on the CV chondrite parent body. The constituent phases of grossite-bearing CAIs show heterogeneous oxygen isotopic compositions, with grossite and perovskite displaying systematically ^{16}O-depleted compositions ($\Delta^{17}O = -12‰$ to $-1‰$) relative to uniformly ^{16}O-rich hibonite and spinel ($\Delta^{17}O = -25‰$ to $-21‰$). Melilite is variably ^{16}O-depleted ($\Delta^{17}O = -25‰$ to

−2‰). The observed oxygen isotopic distribution is interpreted as a result of mineralogically controlled oxygen isotopic exchange with an ^{16}O-poor fluid on the CV chondrite parent body. Collectively, the presence of limited fluids played an important role in preferential alteration of grossite to hercynite and magnetite and various degrees of ^{16}O depletion in grossite, perovskite, and melilite during thermal metamorphism. We conclude that, among refractory phases in the inclusions, grossite was the most susceptible to metasomatic reactions with Fe-rich fluids and the second most susceptible, after perovskite, to oxygen isotopic exchange with an ^{16}O-poor fluid during the thermal history of the CV chondrite parent asteroid.

Keywords: Calcium-aluminum-rich inclusions, grossite, hercynite, transmission electron microscopy, oxygen isotopes

1. INTRODUCTION

Grossite is predicted to condense as the third major phase after corundum and hibonite, and before melilite and spinel, from a cooling gas of solar composition (Ebel and Grossman, 2000; Grossman, 2010). However, since its discovery in a coarse-grained Type A CAI from the reduced CV chondrite Leoville (Christophe Michel-Lévy et al., 1982; Weber and Bischoff, 1994), grossite has been found to be relatively rare, even rarer than hibonite, in refractory inclusions from most carbonaceous chondrite groups, except for CH chondrites (Krot et al., 2019a). Consequently, the nature and origin of grossite and its textural relationship with other refractory phases in CAIs are poorly constrained, although this information can provide unique insights into high-temperature conditions in the early solar nebula. Importantly, none of the previously reported grossite-bearing CAIs was studied using transmission electron microscopy (TEM).

In CV chondrites, where CAIs are usually large and abundant, a very small number of grossite-bearing CAIs has been reported and studied so far. Weber and Bischoff (1994) summarized all occurrences of grossite-bearing CAIs in CV chondrites from the literature, mostly in the abstract format, so that detailed descriptions of these CAIs are commonly lacking. Most of these CAIs are coarse-grained, melilite-rich inclusions that have an igneous texture, indicating crystallization from a melt. Only one CAI, *1623-4*, from Vigarano is a fine-grained, spinel-rich inclusion (FGI), which represents the product of high-temperature nebular condensation (MacPherson et al., 2020). Grossite in coarse-grained CAIs generally occurs as a rare phase

surrounded by melilite. It was briefly noted that in a Vigarano CAI, *VICTA*, grossite appears to have been partially altered to Zn-bearing hercynite [$(Fe,Zn)Al_2O_4$] (Weber and Bischoff, 1994). In contrast, two unusual CAIs from Vigarano and NWA 1934 have been identified to contain grossite as a main constituent phase (Maruyama and Tomioka, 2011; Ma et al., 2011). Maruyama and Tomioka (2011) reported an oval-shaped, hercynite-rich inclusion, *CAFI*, from Vigarano that has a core-mantle-rim structure with an igneous texture. In the *CAFI* core, grossite occurs as minor inclusions in dmitryivanovite (a high-pressure polymorph of $CaAl_2O_4$) together with perovskite and hercynite and in coarse-grained hercynite together with gehlenite and perovskite. In the *CAFI* mantle, grossite-hercynite intergrowths surrounded by a gehlenite layer are embedded within coarse-grained hercynite. In addition, grossite occurs as coarse, porous grains in the rim around *CAFI*, and it has been partially replaced by an amorphous aluminous phase or fine-grained aggregates and veins of hercynite. Ma et al. (2011) described a krotite ($CaAl_2O_4$)-rich inclusion, *Cracked Egg*, from NWA 1934 that also has an oval shape and a compact igneous texture. Layers of grossite, hibonite + spinel, and gehlenite surrounds the krotite-rich core of this CAI. Veins and inclusions of hercynite are commonly associated with grossite and krotite in *Cracked Egg* (Krot et al., 2019a).

Limited oxygen isotopic data for grossite-bearing CAIs from CV chondrites are available in the literature. Krot et al. (2019a) reported a bimodal distribution between ^{16}O-poor grossite, krotite, melilite, and perovskite, and ^{16}O-rich hibonite and spinel in *Cracked Egg*. This isotopic heterogeneity was commonly observed in many CAIs from metamorphosed CV and CO chondrites, and there are various degrees of ^{16}O depletion in grossite, krotite, melilite, and perovskite among different inclusions relative to uniformly ^{16}O-rich hibonite, spinel, and forsterite (e.g., Wasson et al., 2001; Fagan et al., 2004; Itoh et al., 2004; Aléon et al., 2005; Krot et al., 2019a, b; Simon et al., 2019b). This contrasts with grossite-bearing CAIs from the least altered CR2, CO3.0, and CH3 chondrites displaying internally uniform ^{16}O-rich compositions (e.g., Makide et al., 2009; Han et al., 2019; Simon et al., 2019a). Although the origin of heterogenous oxygen isotopic compositions in CAIs remains controversial, the oxygen isotopic heterogeneity observed in FGIs from metamorphosed CV and CO chondrites were widely interpreted as a result of mineralogically controlled oxygen isotopic exchange with an ^{16}O-poor fluid on the chondrite parent asteroids (Wasson et al., 2001; Fagan et al., 2004; Itoh et al., 2004; Aléon et al., 2005; Makide et al., 2009; Krot et al., 2019a, b; Simon et al., 2019b; Krot et al., 2021, 2022).

Here we report the occurrence of grossite in FGIs from three reduced CV chondrites Efremovka, Thiel Mountains (TIL) 07003, and TIL 07007. Coordinated microanalyses of these rare grossite-bearing FGIs were performed to fully characterize the nano-to-micrometer scale mineralogy, petrology, and chemistry of individual inclusions, to document any microstructural and textural relationships between grossite and associated mineral phases, to search for any oxygen isotopic heterogeneities among and within individual inclusions, and to find any correlations between oxygen isotopic compositions and mineralogical and chemical characteristics of individual inclusions. Our goals were to understand the origin of grossite-bearing FGIs from reduced CV chondrites and to decipher processes that they experienced in the solar nebula and on the parent asteroid. Of our particular interest is the spatial association of hercynite (or Al-Fe oxide) with grossite, which was commonly observed in grossite-bearing CAIs from metamorphosed CV and CO chondrites (Weber and Bischoff, 1994; Maruyama and Tomioka, 2011; Krot et al., 2019a; Simon et al., 2019b; Zhang et al., 2020). This Fe-rich phase was interpreted as a secondary low-temperature mineral attributed to fluid-assisted thermal metamorphism on the CO and CV chondrite parent asteroids. We examine the formation conditions of hercynite and any phases associated with grossite to investigate a possible role of fluid-mineral interactions on the CV chondrite parent asteroid.

2. ANALYTICAL METHODS

2.1. Mineralogy and petrology

Based on backscattered electron (BSE) images and full elemental x-ray maps obtained using a JEOL 7600F scanning electron microscope (SEM) at NASA Johnson Space Center (JSC) and a JEOL JXA-8530F electron probe micro-analyzer (EPMA) at Korea Polar Research Institute (KOPRI), we located 63 FGIs from two thin sections each of Vigarano and Efremovka and one each of TIL 07003 and TIL 07007. Only six inclusions contain grossite (Figs. 1–4), including one from Efremovka (*E-B-1*), two from TIL 07003 (*TIL 3-11* and *TIL 3-16*), and three from TIL 07007 (*TIL 7-05*, *TIL 7-08*, and *TIL 7-18*). In comparison, twenty inclusions contain hibonite, and four of them contain grossite. We used a JEOL 7600F SEM and a FEI Quanta 3D 600 dual beam focused ion beam (FIB)/SEM at NASA JSC for the detailed mineralogical and petrologic characterization of these grossite-bearing CAIs. Quantitative wavelength-dispersive analyses were obtained using a JEOL JXA-8530F EPMA at NASA JSC. These measurements were performed

at 15 kV accelerating voltage, 30 nA beam current, and 1 μm spot size. Elemental calibration was carried out using synthetic and natural minerals, and data were reduced using the modified ZAF correction procedure PAP (Pouchou and Pichoir, 1984). The detection limits (in wt%) were 0.01 for SiO_2, Al_2O_3, MgO, CaO, and Na_2O and 0.02 for TiO_2, Cr_2O_3, V_2O_3, FeO, and MnO.

After SIMS measurements, five electron transparent sections were prepared from grossite in four CAIs (*E-B-1*, *TIL 7-05*, *TIL 7-08*, and *TIL 7-18*) using the NASA JSC FIB. The FIB sections were analyzed using a JEOL 2500SE 200 kV field-emission scanning TEM (STEM) at NASA JSC. We obtained bright-field (BF) and dark-field (DF) STEM images, high-resolution (HR) TEM images, and selected area electron diffraction patterns. In addition, elemental mapping and quantitative microanalyses were carried out using a JEOL 60 mm^2 silicon drift detector energy dispersive x-ray (EDX) spectrometer. Elemental x-ray maps were obtained using STEM raster mode with a scanned probe size of 2 nm and a dwell time of 50 μs/pixel. Successive rasters were added until <1% counting statistical errors were achieved for major elements. Data reduction was performed using the Cliff-Lorimer thin film approximation with experimental and theoretical K-factors determined from natural and synthetic standards.

2.2. Oxygen isotopic compositions

Accurate targeting of Cs^+ ion beam onto single mineral phases of interest is vital to obtain precise oxygen isotopic ratios without any overlaps with adjacent phases. Prior to SIMS measurements, FIB marks were etched on the surface of carbon-coated thin sections by using the NASA JSC FIB, following the method described in Nakashima et al. (2012). An ion beam at 30 kV accelerating voltage and 10–30 pA beam current was rastered in a square area of normally 1.5×1.5 μm^2 for up to 2 minutes to remove the surface carbon coating only. After SIMS analyses, the position of the sputtered areas for oxygen isotopic measurements were verified using a JEOL 7600F SEM at NASA JSC.

Oxygen isotopic compositions of grossite-bearing CAIs were analyzed with a Cameca ims-1280 ion microprobe at University of Hawai‘i at Mānoa using the method of Nagashima et al. (2015). A primary Cs^+ ion beam was focused to 2–3 μm with an intensity of ~25 pA. A normal incidental gun was used for charge compensation. Three isotopes of oxygen were measured simultaneously: $^{16}O^-$ was measured using a Faraday cup and $^{17}O^-$ and $^{18}O^-$ were measured using electron multipliers. Instrumental fractionation was corrected using terrestrial standards, including

Madagascar hibonite for hibonite and grossite, San Benito perovskite for perovskite, Burma spinel for spinel, and San Carlos olivine for melilite. Data are reported as deviations from Vienna Standard Mean Ocean Water (VSMOW) in parts per thousand, $\delta^{17,18}O = [(^{17,18}O/^{16}O)_{sample} / (^{17,18}O/^{16}O)_{VSMOW} - 1] \times 1000$, and as deviation from the terrestrial fractionation (TF) line, $\Delta^{17}O = \delta^{17}O - 0.52 \times \delta^{18}O$. Errors represent 2σ analytical uncertainty including the internal measurement precision and the external reproducibility for standard measurements, and they are typically ~1.2‰, ~2.3‰, and ~2.4‰ for $\delta^{18}O$, $\delta^{17}O$, and $\Delta^{17}O$, respectively.

3. RESULTS

3.1. Petrography of grossite-bearing FGIs

The six grossite-bearing FGIs analyzed for this study are typical of FGIs from reduced CV chondrites, as described in Krot et al. (2004). All the inclusions consist of aggregates of irregularly-shaped nodules that show variations in mineralogy, modal abundance, and texture, as described below. Based on our petrographic and mineralogical observations of the FGI nodules, we refer to hercynite as a secondary Fe-rich phase that has partially embayed and replaced grossite, regardless of its variations in Fe, Mg, and Zn concentrations. Primary spinel surrounds grossite and hercynite, and variable atomic Fe/(Fe+Mg) ratios up to 0.4 are observed in the spinel.

E-B-1 is an irregularly-shaped inclusion (1.2 mm in size) dominated by hibonite-spinel-rich nodules having a core of hibonite laths surrounded by spinel, melilite, anorthite, and diopside. Additionally, clusters of rare grossite-rich nodules are distributed in the outer margin of the inclusion; thus, no well-developed concentric zoning structure is apparent. The grossite-rich nodules have a core of grossite surrounded by hercynite, enclosed by ±hibonite, spinel, melilite, and diopside (Figs. 1a-c). Hercynite occurs as thick layers (≤15 μm in thickness) with randomly distributed pores (Figs. 1a, d) and contains numerous inclusions of high-Z nanoparticles (Fig. 1e). Hercynite shares sharp grain boundaries with surrounding spinel, hibonite, and melilite, whereas it displays an irregular, fibrous appearance in contact with grossite, with some regions containing parallel lamellae (Figs. 1d-e). Perovskite occurs as inclusions in grossite, hibonite, and spinel throughout both types of nodules.

Three inclusions, *TIL 3-11*, *TIL 3-16*, and *TIL 7-18* (95 μm, 97 μm, and 180 μm in size, respectively), appear as fragments of larger FGIs (Fig. 2). They share a basic nodular structure (Figs. 2a-c), in which individual nodules have spinel-rich cores surrounded by layers of melilite

and diopside. Grossite occurs in the cores of some nodules; it is partially surrounded by hercynite (typically ≤5 μm in thickness), followed by spinel. Hercynite shares similar textural and chemical features as in *E-B-1*, except that numerous nanometer-sized pores occur aligned in the hercynite, often at high angles to the surface of underlying spinel (Figs. 2d-f). Perovskite is common as inclusions in grossite and spinel in all three CAIs. In *TIL 3-11*, hibonite laths are enclosed by spinel, with only minor contact with grossite (Fig. 2a). A hibonite lath in spinel is observed only in a single, grossite-free nodule of *TIL 7-18*.

TIL 7-05 is an elongated, grossite-spinel-rich inclusion (1.2 mm in size). Most nodules are dominated by spinel surrounded by layers of melilite, ±anorthite, and diopside (Fig. 3a). Grossite surrounded by spinel is observed in a core of the largest nodule, as two relatively large, elongated areas (180 μm and 75 μm in size, respectively) separated by the matrix material (Figs. 3a-b) and as two smaller grains (~12 μm in size) in close proximity (Fig. 3d). Hercynite veins, typically <3 μm in thickness, occur within grossite and at the grossite-spinel grain boundaries (Fig. 3c). The veins often exhibit linear pores through their middle parts. Parallel lamellae of an unknown phase appear as a bright contrast in some regions of grossite (Figs. 3b-c). Perovskite grains are concentrated in the center regions of the largest nodule, and many of them occur adjacent to and within grossite.

TIL 7-08 is a mineralogically zoned, elongated inclusion (2.5 mm in size), which has a Ca-rich core (Fig. 4a) and a Mg-rich mantle (Fig. 4b). The core consists of melilite ± spinel ± hibonite nodules partially separated by thin, discontinuous rims of diopside (Fig. 4a). Some nodules have grossite (<15 μm in size) that occurs as rare irregularly-shaped to rounded grains in melilite (Figs. 4c-f). When present, spinel shares straight grain boundaries with grossite (Fig. 4c). Perovskite occurs in grossite and spinel and at the grossite-melilite grain boundaries (Figs. 4c-d). The CAI mantle is dominated by elongated nodules having cores of spinel and perovskite surrounded by layers of melilite and diopside (Fig. 4b). No hibonite is observed in the mantle.

3.2. Mineral chemistry

Grossite is nearly stoichiometric $CaAl_4O_7$ in all FGIs studied, but typically contains minor to trace FeO contents among the inclusions (Fig. 5a). *TIL 7-08* displays the lowest FeO content, ≤0.1 wt%. *TIL 7-05* contains 0.2–0.5 wt% FeO. Four other CAIs have higher FeO contents, up to 2.7 wt%. Some analyses from *TIL 3-11* and *TIL 3-16* have >1 wt% FeO, which may result from

overlapping with hercynite present underneath the thin section surfaces, as TEM EDX analysis reveals that grossite contains 0.1–0.6 wt% FeO.

Two inclusions, *TIL 7-05* and *TIL 7-08* with grossite that is the most FeO-poor, also contain FeO-poor spinel (Fig. 5b) and melilite. In *TIL 7-08*, spinel (mostly <0.2 wt%) and melilite (≤0.1 wt%) in the core is generally less FeO-rich than those in the mantle (0.2–1.1 wt% and 0.4–0.5 wt%, respectively). In *E-B-1*, spinel in the grossite-rich nodules shows distinctly higher FeO contents with 11.1–17.2 wt% than that in the hibonite-rich nodules having 0.4–3.6 wt% FeO. This is also apparent in melilite chemistry: 0.7–0.9 wt% FeO in the grossite-rich nodules and 0.1–0.6 wt% FeO in the hibonite-rich nodules. FGIs with higher amounts of FeO in spinel tend to show a reduced variability in its Cr_2O_3 contents, although no clear correlation between FeO and Cr_2O_3 contents in spinel is observed. Melilite in *E-B-1* and *TIL 3-11* contains up to 0.4 wt% Na_2O, in contrast to that in other inclusions having <0.2 wt% Na_2O. Elemental Na x-ray maps indicate local enrichments at the outermost edges of melilite in *E-B-1*, *TIL 3-11*, *TIL 3-16*, and *TIL 7-18*, suggestive of minor replacement of primary melilite by nepheline while most melilite remains pristine.

3.3. TEM observations

In the grossite-rich nodules from *E-B-1*, grossite is surrounded by a hercynite layer, consisting of aggregates of numerous micrometer-long laths (Fig. 6a). Most hercynite laths are parallel to each other but some are radially oriented, extending into grossite (Fig. 6d). Magnetite nanoparticles (<200 nm in size), which correspond to high-Z nanoparticles observed in hercynite in BSE images (Fig. 1e), occur at the tips of these hercynite laths, and these two spinel-structured phases are in crystallographic continuity (Fig. 6b). TEM EDX spectra from the magnetite nanoparticles are dominated by Fe with minor contributions of Al and Ca from surrounding hercynite and grossite. Hercynite shares a crystallographic orientation relationship with adjacent grossite, such that $[111]_{hercynite}//[\bar{3}01]_{grossite}$ and $(110)_{hercynite}//(010)_{grossite}$ (Fig. 6c). The hercynite laths are elongated normal to the b direction of adjacent grossite. On the other hand, micrometer-sized hercynite crystals are commonly faceted along the {111} planes, sharing straight grain boundaries with adjacent grossite (Fig. 6d), but without a crystallographic orientation relationship with grossite. A rare hercynite inclusion in grossite is observed, with its face oriented along the (200) plane of the host grossite (Fig. 6e). Finally, Al-rich amorphous material occurs as abundant, commonly porous, lamellae (<100 nm in thickness) alternating with grossite and as patches

interstitially between grossite and hercynite (Figs. 6a, d). Some amorphous lamellae and cracks are oriented parallel to the $(1\bar{3}1)$ and (200) planes of the host grossite (Fig. 6e).

In *TIL 7-18*, grossite is associated with two textural types of hercynite, as well as patches of Al-rich amorphous material. The first type (Figs. 7a-c) is fine-grained aggregates of hercynite grains that form a layer up to ~4 μm in thickness separating grossite from spinel and melilite. These hercynite aggregates share compositionally and texturally sharp grain boundaries with micrometer-sized spinel and melilite grains. In contrast, hercynite in contact with grossite generally displays irregular grain boundaries, similar to those between grossite and the amorphous material. Some hercynite in contact with grossite occurs as nanometer-long, parallel laths that protrude into grossite (Fig. 7d). These hercynite laths are elongated normal to the b direction of adjacent grossite, and there is a crystallographic continuity between these two phases, such that $(110)_{hercynite}//(010)_{grossite}$ (Figs. 7d-e). The tips of the hercynite laths are commonly decorated by magnetite nanoparticles (<50 nm in size; Fig. 7d), as in *E-B-1*. Polygonal pores are also observed at the interfaces between hercynite laths and grossite and along straight grain boundaries between grossite grains (Figs. 7c-d). The second type (Figs. 8a-b) is micrometer to sub-micrometer sized, porous hercynite crystals that occur inside the first textural type, the fine-grained hercynite layer. Pores in these crystals appear step-like and interconnected, and major facets of them are always oriented along {111} of the host hercynite (Fig. 8c). Pores are also developed in the outer regions of grossite and perovskite in contact with porous hercynite crystals (Fig. 8b). FeS-rich nanoparticles (≤50 nm in size; Fig. 8d) are concentrated in the outer regions of some porous hercynite crystals. They are too small to precisely determine, but are likely troilite (Krot et al., 2019a) due to the lack of oxygen x-ray signals in TEM EDX spectra. Perovskite grains are associated with both types of hercynite in this inclusion and share chemically sharp grain boundaries with them. Some perovskite grains appear to have replaced by ilmenite.

In *TIL 7-05*, the Fe-rich veins between grossite grains consist of porous aggregates of blocky to elongated hercynite crystals, and numerous hercynite nanoparticles are also ubiquitous in the veins (Fig. 9a). In addition, the parallel lamellae that appear as brighter layers within some regions in grossite in BSE images (Figs. 3b-c) are Al-rich amorphous material (≤~250 nm in thickness; Fig. 9b).

In *TIL 7-08*, grossite shares highly irregular interfaces with Al-rich amorphous material and with porous aggregates (~3 μm in thickness) of blocky to elongated hercynite grains (Fig. 10).

In contrast, the amorphous material and the hercynite aggregates appear to share sharp grain boundaries with surrounding melilite (Fig. 10a), suggesting that they have grown from the grain boundaries with melilite into grossite.

Our TEM EDX analysis reveals a complexity in hercynite compositions among four grossite-bearing FGIs studied. Hercynite shows a solid solution with spinel and gahnite ($ZnAl_2O_4$), exhibiting different ranges of Mg, Fe, and Zn concentrations among individual inclusions (Fig. 11). Some hercynite grains contain minor MnO (0.2–0.4 wt%). Hercynite in *E-B-1* shows the highest Fe contents, but the lowest Zn contents, compared to other inclusions analyzed; especially, micrometer-sized hercynite crystals are close to an endmember $FeAl_2O_4$, with no detectable Zn. Hercynite in *TIL 7-05* and *TIL 7-18* contains higher Zn contents, but similar Fe contents, compared to that in *E-B-1*. In *TIL 7-18*, porous hercynite grains tend to contain slightly higher Zn contents, but have a wider Fe range than the fine-grained hercynite layer. Finally, *TIL 7-08* contains the lowest Fe contents, but relatively constant Zn contents. With total Fe calculated as Fe^{2+}, many analyses from the four inclusions have Al cation abundances lower than two per formula unit, down to 1.85. This suggests that some of Fe^{3+} are contained in magnetite nanoparticles, as observed in *E-B-1* (Figs. 6b-c) and *TIL 7-18* (Fig. 7d).

Spinel in contact with hercynite in *E-B-1* contains high FeO contents (18 wt%) but is less FeO-rich than adjacent hercynite (32 wt%). In contrast, spinel in three other TIL inclusions is nearly stoichiometric $MgAl_2O_4$, and its center contains relatively uniform FeO contents at <2 wt%. However, Fe and Zn enrichments are observed at the edges of spinel grains adjacent to or near hercynite in *TIL 7-05* and *TIL 7-18* (Figs. 12a-b). A progressive decrease in FeO and ZnO contents occurs over a distance up to 1 μm from the spinel-hercynite and spinel-spinel interfaces, with a typical zoning depth of ≤0.5 μm for FeO and ≤0.2 μm for ZnO (Fig. 12c). The edges of spinel grains have much lower FeO contents, up to 17 wt%, compared to adjacent hercynite (31-38 wt%), but ZnO contents can increase up to 1.5 wt%, comparable to those in hercynite. In addition, the grossite-hercynite grain boundaries in all inclusions are chemically sharp in terms of Fe, Mg, and Zn concentrations, although highly irregular and decorated by pores, because grossite contains only little FeO contents (≤0.6 wt%), but no Zn and Mg.

Perovskite in all four FGIs is nearly pure $CaTiO_3$ with ~0.5–1.5 wt% Al_2O_3. This phase contains very low FeO contents (≤0.6 wt%), even though it is in contact with hercynite. In *TIL 7-18*, two perovskite grains associated with the fine-grained hercynite layers share ragged,

chemically abrupt grain boundaries with ilmenite (Fig. 12b), indicative of a partial replacement of perovskite by ilmenite. When present, pores are preferentially associated only with ilmenite.

The Al-rich amorphous material in all FIB sections is compositionally similar to the host grossite. This material contains 68–92 wt% Al_2O_3 and 3–22 wt% CaO, therefore it is more Al-rich, less Ca-rich, than coexisting grossite. Minor Mg, Fe, and S are also detected in the amorphous material.

3.4. Oxygen isotopic compositions

Oxygen isotopic compositions of individual minerals in grossite-bearing FGIs are listed in Table 1 and plotted in Fig. 13. In all FGIs, spinel and hibonite are uniformly ^{16}O-rich ($\Delta^{17}O$ = −25‰ to −21‰), whereas perovskite is uniformly ^{16}O-poor ($\Delta^{17}O$ = −3‰ to −1‰). Grossite shows less uniform ^{16}O-poor compositions ($\Delta^{17}O$ = −6‰ to −1‰) in all FGIs, except for *TIL 7-08* being slightly less ^{16}O-depleted ($\Delta^{17}O$ = −12‰ to −8‰). As revealed by TEM analyses, grossite in *E-B-1* and *TIL 7-05* is intimately associated with the Al-rich amorphous lamellae (Figs. 6, 9), which could not be avoided during some SIMS measurements, but oxygen isotopic compositions of all spots of grossite in these inclusions are constant within error.

Melilite exhibits heterogeneous oxygen isotopic compositions among and within the FGIs, with large variations in $\Delta^{17}O$ from −25‰ to −2‰. *E-B-1* and *TIL 3-11* show a bimodal distribution in which melilite and grossite have similar ^{16}O-poor compositions ($\Delta^{17}O$ = −6‰ to −2‰), in contrast to ^{16}O-rich hibonite and spinel. In the four other inclusions, melilite displays intermediate compositions between those of ^{16}O-rich spinel and ^{16}O-poor grossite, although each inclusion has distinct ranges. *TIL 3-16* and *TIL 7-18* contain less ^{16}O-depleted melilite ($\Delta^{17}O$ = −18‰ to −13‰ and −9‰, respectively) relative to ^{16}O-poor grossite. In *TIL 7-05*, melilite shows the most heterogeneous compositions, with $\Delta^{17}O$ ranging from −23‰ to −2‰. This range covers two extreme compositions between ^{16}O-rich spinel and ^{16}O-poor grossite and perovskite. *TIL 7-08* exhibits a progressive ^{16}O depletion in the order of the most ^{16}O-rich hibonite and spinel, melilite, grossite, finally to the most ^{16}O-poor perovskite. Melilite is isotopically heterogeneous in this inclusion, with $\Delta^{17}O$ ranging from −25‰ to −12‰.

4. DISCUSSION

4.1. Grossite-bearing FGIs as nebular condensates

Our textural and mineralogical observations of grossite-bearing FGIs in the reduced CV chondrites Efremovka, TIL 07003, and TIL 07007, whether mineralogically zoned or not, can be interpreted as evidence for a condensation origin. As shown in Figs. 1-4, these include: (1) individual nodules within the inclusions typically show irregular shapes and well-developed layered structures; (2) distinctive mineral layers of the nodules share highly curved and irregular interfaces and consist of fine-grained, randomly-oriented crystals of refractory phases. These observations provide textural evidence against an igneous origin. Importantly, (3) each of the nodules shares a similar mineral sequence of primary refractory phases, which become less refractory outwards from their core. Based on the apparent mineral layer sequence observed from grossite-bearing FGIs studied, we infer sequential condensation of perovskite, followed by grossite, hibonite, spinel, melilite, diopside, and finally anorthite to lower temperatures. This texturally inferred sequence is overall inconsistent with the predicted equilibrium condensation sequence (Ebel and Grossman, 2000; Grossman, 2010), in particular the reversed sequence of grossite relative to hibonite, as discussed below. Our interpretation is consistent with the widely held view of FGIs representing aggregates of high-temperature condensates in the early solar nebula, which was concluded by previous studies of FGIs in carbonaceous chondrites that are mostly grossite-free (e.g., Krot et al., 2004, 2019a; Han and Brearley, 2017; Han et al., 2019; Simon et al., 2019a; Che and Brearley, 2021).

Our data indicate the formation of grossite before hibonite, but this conflicts with equilibrium condensation models that predict condensation of hibonite before grossite (Ebel and Grossman, 2000; Grossman, 2010). One possibility is that conditions during grossite condensation were different from those assumed in these models. For example, a super-cooled nebular gas under disequilibrium conditions may have enabled a rapid, incomplete condensation of perovskite and grossite, instead of direct condensation of corundum or hibonite by homogenous nucleation (Petaev and Wood, 2005). Alternatively, a nebular gas reservoir from which grossite was condensing may have been enriched in Ca relative to Al with respect to the solar composition. This was suggested by Kimura et al. (1993) and Weber and Bischoff (1994) who observed that bulk Ca/Al ratios are higher in grossite-rich CAIs in CH chondrites than in spinel-hibonite inclusions in CM chondrites. By utilizing the condensation with partial isolation code of Petaev and Wood (1998), Ivanova et al. (2002) demonstrated that elevated Ca abundances by a factor of 5 or more compared to the solar composition can increase the stability of grossite (and krotite). In addition,

previous equilibrium condensation models showed that enhanced dust/gas ratios or high nebular gas pressure can increase the stability of grossite as well (Yoneda and Grossman, 1995; Ebel and Grossman, 2000; Ivanova et al., 2002). Collectively, we conclude that grossite-bearing FGIs record localized condensation episodes from a heterogeneous gas reservoir with variable physico-chemical properties, which were not prevalent throughout the early solar nebula. In addition, the rarity of grossite in CV chondrites may have resulted from its greater susceptibility to fluid-driven metasomatic reactions than any other CAI minerals, as discussed in Section 4.2.2.

4.2. Parent body alteration of grossite-bearing FGIs

Grossite-bearing FGIs in Efremovka, TIL 07003, and TIL 07007 show mineralogical and chemical characteristics that are a result of secondary parent body alteration, although their primary mineralogy and structure have not been completely modified by such alteration, as discussed in Section 4.1. These include: (1) the common occurrence of Zn-bearing hercynite, sometimes with magnetite nanoparticles, and Al-rich amorphous material that are preferentially restricted to grossite (Figs. 6-10); (2) increased FeO contents in grossite and spinel grains (Fig. 5) and correlated Fe and Zn enrichments at the edges of spinel grains adjacent to the grossite and hercynite alteration assemblages (Fig. 12); and (3) the minor occurrence of ilmenite on the exterior of perovskite grains (Fig. 12b). These observations can be interpreted as the effects of metasomatism and metamorphism in the parent body environment (e.g., Bonal et al., 2020), where a fluid was capable of mobilizing Al, Ca, Fe, Mg, and Zn among all the components in CV chondrites (Brearley and Krot, 2013). Below we examine the conditions of secondary parent body alteration that affected the mineralogical and chemical evolution of grossite-bearing FGIs in reduced CV chondrites.

4.2.1. Formation of hercynite and magnetite

An important observation in this study is that grossite is preferentially embayed by hercynite and ±magnetite (Figs. 6-10), indicating that the former has been partially replaced by the latter. A condensation origin for hercynite and magnetite can be rejected for several reasons. If condensation was responsible, hercynite and magnetite should have formed as the outermost layer surrounding diopside, rather than between grossite and spinel, because they are predicted to condense at much lower temperatures than any refractory phases observed in FGI nodules (<500

K at 10^{-3} bar; Grossman, 1972; Wood and Hashimoto, 1993). Thermodynamic calculations showed that fayalite contents in chondritic olivine are much higher than can be produced during condensation in a solar or even highly oxidizing nebular gas (Fedkin and Grossman, 2006), implying that condensation of gaseous Fe and Al into hercynite is also unlikely. In addition, the increased ZnO contents (up to 1.7 wt%) in hercynite are difficult to explain by a condensation origin. Zinc is a moderately volatile element and it is compatible in Mg silicates. Instead of spinel (or hercynite), forsterite and enstatite are predicted to serve as the host phases for initial condensation of a trace amount of Zn at much lower temperatures (by ~600 K; Lodders, 2003) than diopside condensation.

Conclusive evidence against a nebular origin of hercynite and magnetite is also provided by a comparison with grossite-bearing CAIs from pristine carbonaceous chondrites of petrologic subtype 3.0 that do not contain any similar type of Fe-rich oxide phases. These include DOM 08006 (CO3.0; Simon et al., 2019a; Zhang et al., 2020), as well as CH3 chondrites (Kimura et al., 1993; Weber and Bischoff, 1994; Ivanova et al, 2002; Krot et al., 2019a). In contrast, hercynite is present, preferentially with grossite, in all grossite-bearing CAIs from reduced CV chondrites we studied, as well as those in carbonaceous chondrites of petrologic subtype higher than 3.0, which include Yamato 81020 and Colony (CO3.05; Krot et al., 2019a; Zhang et al., 2020), DOM 08004 and MIL 090010 (CO3.1; Simon et al., 2019b; Zhang et al., 2020), and Vigarano (CV3.1–3.4; Weber and Bischoff, 1994; Maruyama and Tomioka, 2011). The occurrence of magnetite nanoparticles has not been previously reported from any grossite-bearing CAIs, possibly due to their fine size that is difficult to resolve by SEM and EPMA. However, magnetite was observed as complex opaque assemblages with metallic and sulfide phases in CAIs from CV chondrites, mostly Allende, which likely formed by secondary exsolution, oxidation, and sulfurization alteration of metal alloys on the parent body (Blum et al., 1989). Collectively, we infer that the occurrence of hercynite and magnetite in grossite-bearing FGIs is the product of secondary alteration processes on the parent body (Maruyama and Tomioka, 2011; Krot et al., 2019a; Simon et al., 2019b; Zhang et al., 2020). This is further evidence for the mobilization and redistribution of Fe, Mg, Zn, Al, and Ca during such processes.

Distinctive textural and chemical relationships between grossite and hercynite can be attributed to a fluid-driven dissolution-precipitation process (Putnis, 2009). Pores are widespread along hercynite and grossite grain boundaries and within hercynite grains (Figs. 6-10). In particular,

pores within hercynite are interconnected and aligned (Figs. 8a-c), likely forming channels for fluid flow and element transport. Grossite shares highly embayed, irregular grain boundaries with hercynite (Figs. 6-10), suggestive of their reaction relationship. Hercynite often exhibits lath-like morphology (Figs. 6a, 6d, 7d), which indicates that hercynite has progressively grown into grossite grains at the expense of grossite. Hercynite displays sharp compositional boundaries with grossite, especially with respect to Fe, Mg, Zn, and Ca contents (Figs. 6b, 7b, 9a), with no evidence for diffusional exchange between these two phases even on the nanometer scale. We therefore infer that, as a response to thermal metamorphism, aqueous fluids enriched in Fe and Zn became available to have partially dissolved primary grossite, resulting in the precipitation of secondary hercynite and magnetite as well as the development of abundant pores.

An important question is a source of Al, Mg, Fe, and Zn to form hercynite and magnetite that have partially replaced grossite. Aluminum in hercynite likely has a local origin; that is, dissolution of grossite released Al to fluids. It is also plausible that little Al was lost and transported in the presence of fluids during metasomatic alteration of primary melilite replaced by nepheline (e.g., Han et al., 2022) and subsequently incorporated into hercynite. The high Mg contents in hercynite (up to 25 wt%, but mostly <10 wt% MgO) likely require Mg to be supplied externally by fluids. An external source of all Fe is required because primary phases were originally FeO-poor, and therefore it is highly likely that Fe was delivered by the aid of fluids equilibrated with the matrix. Magnesium and Fe may have been mobilized during metamorphic crystallization of ferrous olivine from amorphous silicates, the dominant constituent in the matrix from pristine carbonaceous chondrites, in the presence of limited fluids (Abreu and Brearley, 2011). All Zn must also have been derived externally, possibly from troilite or silicate (Kimura et al., 2006). Johnson and Prinz (1991) and Kimura et al. (2006) observed a broad correlation of ZnO contents in spinel/chromite in chondrules with petrologic subtype of CO3 and L/LL chondrites. Similarly, Kornacki and Wood (1985) showed a positive correlation between ZnO and FeO contents in spinel that contains >10 wt% FeO in altered FGIs from Allende. These studies demonstrated that Zn was mobilized and redistributed during thermal metamorphism. Overall, substantial element exchange between FGIs and the surrounding matrix occurred during a grossite alteration event, emphasizing the important role of aqueous fluids in this exchange.

The metasomatic replacement reaction of grossite by hercynite and magnetite can be described via the coupling of dissolution of grossite and subsequent precipitation of hercynite and

magnetite in the presence of fluids (Putnis, 2009), as follows:

$$CaAl_4O_{7(s)} + H_2O_{(aq)} = Ca^{2+}_{(aq)} + 4AlO_2^-{}_{(aq)} + 2H^+_{(aq)}$$
$$2AlO_2^-{}_{(aq)} + Fe^{2+}_{(aq)} + 2H^+_{(aq)} = FeAl_2O_{4(s)} + H_{2(g)}$$
$$3Fe^{2+}_{(aq)} + 10H_2O_{(aq)} = Fe_3O_{4(s)} + 6OH^-_{(aq)} + 7H_{2(g)}$$

Melting of ice produced fluids that were introduced along grain boundaries, initiating grossite dissolution and releasing Al into the fluids. This process provided a strong control on local fluid compositions. As the resulting fluids became supersaturated with respect to a hercynite composition, the first hercynite precipitates nucleated and grew as numerous and nanometer-sized crystals on the surface of surrounding refractory phases (e.g., spinel). As a reaction front with the fluids was gradually advancing into the interiors and along the grain boundaries of dissolving grossite grains, continuous precipitation and inward growth of hercynite proceeded by consuming Al in the fluids and so promoted further dissolution of grossite. The porosity was also produced during this dissolution-precipitation process, and pores (as well as grain boundaries and cracks) acted as an effective pathway for fluid infiltration and element transport to and from the inward moving reaction front with as yet unreacted, primary grossite. In the final stage, minor magnetite nanoparticles precipitated onto the exposed surfaces of hercynite at the limit of infiltrating fluids. Meanwhile, the outgoing fluids must have involved the efficient removal of Ca released from dissolving grossite during hercynite crystallization. This Ca was likely precipitated as Ca-Fe silicates outside the host CAIs by interaction with fluids enriched in Fe, Mg, and Si (e.g., Che and Brearley, 2021; Krot et al., 2021). For example, Ca enrichments are evident in the matrix adjacent to grossite-rich nodules on *E-B-1* (Fig. 1e).

Our TEM observations indicate that the nucleation and growth of precipitating hercynite was crystallographically controlled by grossite. These include the crystallographic orientation relationships of grossite with hercynite and magnetite (Figs. 6c, 7d-e), the occurrence of oriented hercynite laths, commonly at high angles to the surface of underlying spinel (Figs. 6a, 7d), and the oriented and aligned pores along hercynite grain boundaries and within hercynite (Figs. 7d, 8a-c). Moreover, grossite contains parallel amorphous lamellae and cracks developed along preferential crystallographic directions (Figs. 6e, 9b). Therefore, the replacement reaction of grossite by hercynite was epitaxial (Putnis, 2009). In addition, the formation of magnetite was also a result of

a crystallographically-controlled process, i.e., a topotaxial overgrowth onto hercynite.

4.2.2. Grossite alteration during metamorphism

We envision possible scenario(s) for metasomatic replacement alteration of grossite by hercynite and magnetite in relation to the metamorphic history of the CV chondrite parent body. A key in controlling the extent of this fluid-driven alteration is metamorphic temperature and duration, which would largely affect the fluid availability and cooling rate after peak metamorphism.

During an initial stage of increasing metamorphic temperature (i.e., prograde metamorphism), ices that accreted together with the matrix began to melt, enabling aqueous fluids to transport soluble elements and facilitate reactions with CAI minerals. During this initial heating period, the replacement of grossite by hercynite was likely induced by metasomatic reactions at elevated local water/rock ratios and under oxidizing conditions of fluids enriched in Fe, Mg, and Zn. Based on thermodynamic models of aqueous alteration reactions in CI and CV chondrites (Zolotov et al., 2006; Zolotov, 2012; Krot et al., 2021), a high mobility of Fe, Mg, Zn, and Ca required during hercynite formation can be achieved in the presence of aqueous fluids under acidic conditions caused by melting of HCl-bearing ices. As the grossite alteration progressed by releasing Ca, these early acidic fluids were consumed through precipitation of hercynite, possibly resulting in the evolution to neutral to alkaline fluids having the reduced solubility of Fe, Mg, and Zn (Zolotov, 2012). In addition, aqueous fluids enriched in Fe, Mg, and Zn may have supplied Na required during a limited replacement of melilite by nepheline (Zolotov, 2012; Krot et al., 2021).

The low-temperature early stage of grossite alteration on the CV chondrite parent body is supported by previous studies of hydration experiments on calcium aluminate cements composed mainly of various Ca,Al-oxides including krotite and grossite (Pöllmann, 2012). Grossite (and krotite) were experimentally demonstrated to begin to dissolve readily within the first 48 hours of mixing with pure water at water/rock ratios of 0.3–1.58 and at temperatures as low as 4°C up to 120°C, and such dissolution reaction lasted up to several months (Edmonds and Majumdar, 1989; Schmitt et al., 2000; Klaus et al., 2013; Duran et al., 2016). In particular, Klaus et al. (2013) noted a complete dissolution of grossite after few days of hydration at 23°C and a water/rock ratio of 0.45. Although experimental constraints on hydrothermal alteration of grossite are lacking, increasing temperature and water content is generally expected to increase the rate of chemical

reaction between solids and liquids and mass transport, so does the overall degree of hydration (Ukrainczyk, 2010; Pöllmann, 2012; Duran et al., 2016). We therefore infer that a rapid metasomatic replacement of grossite by hercynite began as soon as ices melted and proceeded on a short time scale of days up to months. The limited availability of aqueous fluids was an important limiting factor for complete dissolution of grossite as the fluids were progressively consumed through grossite alteration and also lost with increasing metamorphic temperature. It is possible that the presence of Ca, Mg, Zn, and Na cations in limited amounts of aqueous fluids may have accelerated the dissolution of grossite during the low-temperature (<100°C) early stage of metasomatic alteration, as experimentally proven during the hydration of krotite (Matusinović and Vrbos, 1993; Pöllmann, 2012; Duran et al., 2016).

Furthermore, previous studies of hydration experiments on calcium aluminate cements revealed that the dissolution of grossite led to the simultaneous formation of poorly crystalline to amorphous hydrate phases with various Ca/Al ratios and increased porosity (Pöllmann, 2012). The major products of the hydrate phases were compositionally matched with CAH10, C3AH6, and AH3, where CaO=Ca, Al_2O_3=Al, and H_2O=H (Edmonds and Majumdar, 1989; Klaus et al., 2013; Duran et al., 2016). These phases can be dehydrated and decomposed to crystalline Ca,Al-oxide phases by heating at a temperature range of ~100–300°C (Ukrainczyk et al., 2007). Therefore, we interpret that the occurrence of Al-rich amorphous material with grossite (Figs. 6, 9b, 10a) represents an intermediate stage in which grossite was partially dissolved through interaction with limited Fe-rich fluids and the resulting amorphous Ca,Al-hydrates were subsequently dehydrated by progressive metamorphic heating (Maruyama and Tomioka, 2011).

In comparison, previous hydrothermal experiments of gehlenite at 200°C and a water/rock ratio of 46.7 for 7 days performed by Nomura and Miyamoto (1998) and Ichimura et al. (2017) demonstrated that melilite was partially to completely dissolved and replaced by Na-hydrates in the presence of alkaline aqueous fluids enriched in Na and Si. The major hydrate products include analcime ($NaAlSi_2O_6•H_2O$), nepheline hydrate ($NaAlSiO_4•1/2H_2O$), and hydroxycancrinite ($Na_8Al_6Si_6O_{24}(OH)_2•3H_2O$). However, Nomura and Miyamoto (1998) showed that gehlenite remained unaltered in the presence of pure water, suggesting that gehlenite is more resistant to fluid-driven metasomatic reactions than grossite. We infer that the minor replacement of melilite by nepheline occurred in a later higher-temperature (<300°C) stage of metasomatic alteration when acidic aqueous fluids enriched in Fe, Mg, and Zn had evolved to become more neutral as grossite

alteration progressed and water/rock ratios decreased. In addition, Nomura and Miyamoto (1998) and Ichimura et al. (2017) concluded that nepheline coexisting with melilite in CAIs formed through dehydration of Na-hydrates by progressive metamorphic heating at ~300–700°C for a longer duration of <1 year up to ~10 Ma.

The formation of magnetite after hercynite may have occurred during a transition from aqueous alteration to thermal metamorphism. Thermodynamic calculations by Zolotov et al. (2006) illustrated that magnetite can form during a transition between aqueous and metamorphic conditions and its stability becomes diminished quickly with decreasing water/rock ratio after a complete transition to metamorphic condition. An advanced stage of prolonged and/or higher-temperature metamorphism can lead to the formation of fayalite and Fe-metal at the expense of magnetite (Zolotov et al., 2006; Jogo et al., 2009). Therefore, we infer that magnetite nanoparticles precipitated shortly before fluids became completely consumed or lost at peak metamorphic heating, but may not have continued to grow on fast cooling from peak metamorphism. Alternatively, magnetite may have formed in limited amounts of fluids during cooling after peak metamorphic heating (i.e., retrograde metamorphism). However, with decreasing temperature, the solubility and dissolution and diffusion rates of Fe in fluids decrease as well. Therefore, the precipitation of magnetite from the remaining Fe-rich fluids may have become kinetically limited.

Overall, the survival of primary grossite implies a limited availability of fluids and the short duration and low temperature of metasomatic alteration. If grossite remained in contact with fluids, hercynite continued to grow with time and/or heating in the inward migration of the reaction front with grossite. In addition, the heterogenous compositions of hercynite observed within the FGIs (Fig. 11) reflect nanometer scale variations in fluid chemistry during hercynite crystallization, owing to inefficient mixing in the fluids during metasomatic alteration for a short duration and/or at low temperatures. Importantly, after the formation of hercynite and magnetite, any subsequent metamorphic heating must have proceeded at low temperatures (e.g., ~300–400°C; Huss et al., 2006), followed by rapid cooling, to prevent further textural and chemical equilibration between hercynite and grossite, grain coarsening of hercynite and magnetite, and pore closure. This inference is also supported by the preservations of steep Fe and Zn enrichments on the nanometer scale at the edges of spinel grains adjacent to hercynite (Fig. 12), as discussed in Section 4.2.3. The occurrence of Al-rich amorphous patches and lamellae with grossite (Figs. 6, 9b, 10a) indicates that this material never experienced progressive solid-state crystallization at increasing

metamorphic temperature. Likewise, previous TEM studies of the Vigarano matrix (Lee et al., 1996; Abreu and Brearley, 2011) concluded that aqueous fluids were limited during mild metamorphic heating on the parent body, based on the occurrence of minor smectite and the heterogenous morphologies and compositions of FeO-rich olivines.

Variations in hercynite texture, size, and composition are observed among grossite-bearing FGIs, suggestive of heterogenous degrees and styles of grossite alteration. In *TIL 7-05*, hercynite occurs exclusively as veins (Figs. 3, 9), which likely is a result of the larger size of nodules and grossite grains, compared to other inclusions. In the FIB sections, *TIL 7-05* contains grossite grains ranging in size from 3 μm to 10 μm, whereas the size of grossite grains in *TIL 7-08* and *TIL 7-18* does not exceed 5 μm and is mostly less than 3 μm. In contrast, the hercynite veins in *TIL 7-05* form up to 3 μm in thickness, comparable to the size of hercynite layers and crystals in *TIL 7-18* (Figs. 7-8). On the other hand, grossite in *E-B-1* is surrounded by thicker layers composed of coarser hercynite and magnetite with larger, but less abundant pores (Figs. 1, 6), in comparison with that in all other inclusions. In addition, this refractory phase is in contact with faceted hercynite crystals having nearly a pure $FeAl_2O_4$ composition (Figs. 6d, 11) and contains abundant amorphous lamellae (Fig. 6). These observations suggest that this inclusion experienced more advanced degrees of metasomatic alteration, possibly at higher temperatures and/or for a longer duration. This interpretation is supported by the bimodal distribution of oxygen isotopic compositions observed in *E-B-1*, as discussed in Section 4.3. Lastly, *TIL 7-08* is characterized by a much lower abundance of hercynite and its lower Fe concentrations than other FGIs (Figs. 10-11), which likely reflects a difference in primary mineralogy and bulk composition among the FGIs and a distance of grossite from the matrix. As initial Fe-rich fluids equilibrated with the matrix were pervasively infiltrating into grossite in the core of *TIL 7-08*, the fluids may have become less Fe-rich and lower in abundance through interaction with melilite and spinel in the mantle of this inclusion. This chemical evolution in the fluids is hinted at by the decrease in FeO contents in spinel and melilite from the mantle to the core.

4.2.3. Alteration of spinel and perovskite

The Fe enrichments in primary spinel have been well documented from CAIs in metamorphosed CO and CV chondrites, which are generally interpreted as an indicator of Mg^{2+}-Fe^{2+} diffusive exchange with the surrounding matrix during thermal metamorphism (Huss et al.,

2006). This exchange was accompanied by redistribution and equilibration of Cr in spinel, as indicated by the reduced variability in its Cr_2O_3 contents with increasing FeO contents (Fig. 5b). Such immediate mobilization and redistribution of Cr with the onset of thermal metamorphism was demonstrated based on systematic variations in distribution of Cr_2O_3 contents in olivine in type II chondrules and amoeboid olivine aggregates with increasing petrologic subtype of ordinary and CO3 chondrites (e.g., Grossman and Brearley, 2005; Han et al., 2022). However, our chemical data indicate that Fe enrichments in spinel was aided by the presence of Fe-rich fluids during diffusion process induced by metamorphic heating. For example, in *E-B-1*, spinel adjacent to hercynite in grossite-rich nodules contains significantly higher FeO contents than that in hibonite-spinel-rich nodules (Fig. 5b). This implies that spinel underwent a more extensive degree of chemical equilibration enhanced by Fe-rich fluids as the grossite-fluid interaction was proceeding to form hercynite.

In addition, our TEM EDX analyses of *TIL 7-05* and *TIL 7-18* reveal correlated Fe and Zn enrichments at the edges of spinel grains adjacent or close to hercynite, in contrast to relatively uniform, lower FeO contents with no Zn in their interior (Fig. 12). Owing to a fast Mg-Fe interdiffusion rate in spinel (Liermann and Ganguly, 2002), a diffusion distance of Fe in spinel for 1 Ma at 400°C is ~10 μm, larger than the actual size of spinel grains (typically ≤10 μm in size) in grossite-bearing FGIs. Thus, chemical equilibrium may have been reached to produce the elevated FeO contents throughout spinel grains during peak metamorphic heating, when volume diffusion became dominant so that Fe diffused into the center of spinel grains. Although there are no available experimental data for a Zn diffusion rate in spinel, previous studies of spinel compositions demonstrated the mobilization and redistribution of Zn and its preferential incorporation into spinel in response to thermal metamorphism (Kornacki and Wood, 1985; Johnson and Prinz, 1991; Kimura et al., 2006), as discussed in Section 4.2.1. However, spinel in the Kainsaz CO3.2 chondrite does not contain detectable ZnO contents, but is more FeO-rich than that in the ALHA77307 CO3.0 chondrite (Johnson and Prinz, 1991). Kornacki and Wood (1985) reported that spinel only with >10 wt% FeO in altered FGIs from Allende contains minor ZnO contents up to 0.5 wt%. These observations suggest that diffusion of Zn was limited relative to that of Fe during thermal metamorphism, even at peak metamorphic temperatures up to 700°C estimated for Allende (Huss et al., 2006; Brearley and Krot, 2013). Likewise, narrower zoning depths of Zn than Fe are observed at the edges of spinel grains in *TIL 7-18* (Fig. 12c). In general,

reduced CV chondrites, including Efremovka, are assigned as petrologic subtype 3.1–3.4, lower than Allende that is considered as petrologic subtype greater than 3.6 (Bonal et al., 2006). Under lower degree metamorphic conditions that reduced CV chondrites experienced (Brearley and Krot, 2013), diffusion of Zn into spinel would be more limited. Therefore, the development of correlated Fe and Zn enrichments at the edges of spinel grains requires the presence of aqueous fluids that efficiently delivered Zn together with Fe along spinel grain boundaries. We conclude that Fe and Zn diffused together into spinel in the presence of aqueous fluids enriched in Fe and Zn that was infiltrating into, and interacted with, grossite to form hercynite.

The Fe and Zn enrichments in a narrow zone along spinel grain boundaries could have formed during relatively lower-temperature, short-lived heating event with a limited availability of aqueous fluids on a local scale. This steep zonation could have developed readily as fluids begun to move and transport Fe and Zn cations in the early stage of thermal metamorphism, but preserved by fast cooling after peak metamorphic heating at relatively low temperatures. Alternatively, on cooling after peak metamorphism, Fe and Zn exchange may have occurred at low temperatures before fluids were exhausted. Systematic analyses of spinel compositions in reduced CV chondrites and experimental determination of the Zn diffusivity in spinel are required to better examine the behavior of Zn and its correlation with Fe during thermal metamorphism.

The Fe metasomatic alteration had a minor effect on the replacement reaction of perovskite by ilmenite. Regardless of their close spatial association with hercynite, most perovskite grains are nearly pure $CaTiO_3$ with low FeO contents (≤0.6 wt%), consistent with TEM EDX data of perovskite in melilite-rich FGIs from ALHA77307 (CO3.0) (Han and Brearley, 2017). This indicates a minimal Fe^{2+}-Ca^{2+} diffusive exchange during thermal metamorphism. The sharp compositional boundaries between perovskite and ilmenite and the preferential association of pores with ilmenite in *TIL 7-18* (Fig. 12b) suggest that partial dissolution of perovskite and subsequent precipitation of ilmenite occurred via interaction with Fe-rich fluids. During this interaction, pores formed due to the volume reduction from perovskite to ilmenite and/or more perovskite being dissolved than ilmenite precipitated. This alteration process may have occurred during or after the formation of hercynite, depending on the fluid chemistry (e.g., the solubility and dissolution rates of Ca and Fe).

4.3. Oxygen isotopic heterogeneity

Six grossite-bearing FGIs analyzed in this study show internal oxygen isotopic heterogeneity, in that hibonite and spinel are always ^{16}O-rich compared to ^{16}O-poor grossite and perovskite while melilite varies widely in composition covering the two extreme compositions (Fig. 13). These results are in contrast to uniform ^{16}O-rich compositions ($\Delta^{17}O \approx -24‰$) of grossite-bearing inclusions from the least altered CR, CO3.0, and CH3 chondrites, which represent a record of primordial ^{16}O-rich composition in the CAI-forming region (Makide et al., 2009; Krot et al., 2019a, Simon et al., 2019a). Importantly, Simon et al. (2019a, b) reported contrasting oxygen isotopic compositions of grossite-bearing CAIs between DOM 08006 (CO3.0) and DOM 08004 (CO3.1). Grossite-bearing CAIs from DOM 08006 show uniform ^{16}O-rich compositions falling into a narrow $\Delta^{17}O$ range from −25‰ to −20‰. In contrast, those in DOM 08004 are isotopically heterogeneous in that grossite and melilite are ^{16}O-depleted, ranging in $\Delta^{17}O$ from −11‰ to ~0‰ and from −23‰ to ~0‰, respectively, while hibonite, spinel, and diopside have nearly identical ^{16}O-rich compositions with $\Delta^{17}O$ = −25‰ to −23‰. Similar oxygen isotopic trends are common both in grossite-bearing and grossite-free FGIs from metamorphosed CO and CV chondrites (Wasson et al., 2001; Fagan et al., 2004; Itoh et al., 2004; Aléon et al., 2005; Krot et al., 2019b; Zhang et al., 2020). Thus, we conclude that the observed mineralogically controlled oxygen isotopic heterogeneity of grossite-bearing FGIs from reduced CV chondrites is a result of oxygen isotope exchange with an ^{16}O-poor fluid in the parent body setting after their initial formation by condensation in an ^{16}O-rich gas reservoir.

Based on our oxygen isotope data (Table 1; Fig. 13), perovskite was the most susceptible to oxygen isotopic exchange, and grossite was more susceptible than melilite. This is contrast with grossite being the most susceptible to fluid-driven metasomatism among any refractory minerals, as discussed in Section 4.2. Oxygen diffusivity in perovskite is much faster than that in melilite (Yurimoto et al., 1989; Ryerson and McKeegan, 1994; Bak et al., 2004; Robens et al., 2022), for example, ~$10^{5–10}$ times faster at peak metamorphic temperatures (300–400°C) estimated for reduced CV chondrites (Huss et al., 2006). Perovskite (typically <5 μm in size) in grossite-bearing FGIs is expected to have experienced complete oxygen isotopic exchange even at 300°C under dry conditions on a short time scale (i.e., up to a few days). In contrast, larger gehlenitic melilite grains (typically <10 μm in size) would have undergone little or no oxygen isotopic exchange at 300–400°C under dry conditions for 1 Ma. Although there are no available experimental data for oxygen diffusion rate in melilite under wet conditions, oxygen diffusion rates in olivine and anorthite under

wet conditions were experimentally shown to be 10–70 times and $10^{5–6}$ times faster, respectively, compared to those under dry conditions (Elphick et al., 1988; Costa and Chakraborty, 2008). If oxygen diffusion rate in melilite under wet conditions was enhanced by similar orders, melilite would have experienced partial to complete equilibrium with an ^{16}O-poor fluid during metamorphic heating at 300–400°C for 1 Ma. Thus, the observed heterogeneous oxygen isotopic compositions of melilite may reflect very localized exchange with an ^{16}O-poor fluid, which can be attributed to a limited availability of the fluid. There are no available experimental data for oxygen diffusion rate in grossite, which would help us to better understand the origin of oxygen isotopic heterogeneities in CV CAIs.

Our conclusion is further supported by a correlation between the degree of secondary parent body alteration of grossite-bearing FGIs and their oxygen isotopic compositions. For example, *E-B-1* contains thicker and less porous hercynite layers with abundant magnetite nanoparticles (Figs. 1, 6) and the highest FeO contents in spinel and hercynite (Figs. 5b, 11). This inclusion shows a bimodal distribution between ^{16}O-poor grossite and melilite and ^{16}O-rich hibonite and spinel (Fig. 13b). On the other hand, *TIL 7-08* contains minor hercynite aggregates (Fig. 10) and the lowest FeO contents in grossite, spinel, and hercynite (Figs. 5, 11). In this inclusion, grossite is less ^{16}O-depleted than that in other inclusions, and melilite exhibits a range extending from ^{16}O-rich composition similar to spinel and hibonite to ^{16}O-depleted composition similar to grossite (Fig. 13b). Similarly, a good correlation was inferred based on progressive ^{16}O depletion and FeO increase in melilite in CAIs with increasing petrologic subtype (i.e., the degree of metamorphic grade) of CO3 chondrites (Wasson et al., 2001; Itoh et al., 2004). This correlation indicates that fluid-assisted thermal metamorphism on the CV chondrite parent asteroid played an important role in modifying oxygen isotopic compositions of perovskite, grossite, and melilite in grossite-bearing FGIs.

Compositional constraints on the source of ^{16}O-poor compositions further indicate that the observed oxygen isotopic heterogeneity in grossite-bearing FGIs were established during interaction with aqueous fluids in an asteroidal setting. Krot et al. (2019b) constrained the Δ^{17}O value of fluids as to be −1.5±1‰, inferred from oxygen isotopic compositions of fayalite and magnetite in Kaba (Bali-like oxidized CV3.1) that formed in the presence of fluids during metasomatic alteration at ~200–300°C on the parent body (Zolotov et al., 2006; Brearley and Krot, 2013). Oxygen isotopic compositions of fluids in reduced CV chondrites have not been constrained

yet, although secondary aqueously formed phases, for example, kirschsteinite ($CaFeSiO_4$), occur around CAIs in this group (MacPherson and Krot, 2014). Similarly, our perovskite data have nearly constant $\Delta^{17}O$ values of ~−2‰ and plot along or close to the mass-dependent fractionation line of a slope of ~0.5 (Fig. 13). Grossite in all FGIs but *TIL 7-08* are within or close to the $\Delta^{17}O$ values of fayalite and magnetite in Kaba. All melilite data in *E-B-1* and *TIL 3-11* and the most ^{16}O-poor melilite compositions in *TIL 7-05* also share similar $\Delta^{17}O$ values around −1.5‰. We therefore infer that an ^{16}O-poor fluid interacted with grossite-bearing FGIs on the parent body and modified oxygen isotopic distributions among their constituent minerals.

5. CONCLUSIONS

Our coordinated TEM and SIMS analyses of rare grossite-bearing FGIs from reduced CV chondrites provide new insights into secondary parent body processes that partially altered primary mineralogy and chemical and isotopic compositions of the inclusions. These analyses offer further evidence for the presence of aqueous fluids during the metamorphic history of the CV chondrite parent asteroid. The fluids played an important role in mobilizing Al, Ca, Fe, Mg, and Zn and facilitating oxygen isotopic exchange during metamorphism. Grossite was more susceptible to alteration via interaction with the fluids, compared to other refractory phases in the inclusions.

In the FGIs, grossite occurs in the cores of the nodules, embayed by texturally and chemically diverse and porous hercynite and magnetite nanoparticles. This indicates that grossite has been preferentially replaced by hercynite and magnetite, while pores formed. This replacement reaction was a crystallographically-controlled, fluid-driven process involving partial dissolution of grossite and subsequent precipitation of hercynite and magnetite. This process may have been accompanied by the development of correlated Fe and Zn enrichments on the nanometer scale along spinel grain boundaries. The metasomatic alteration of grossite and spinel likely occurred under fluid-limited conditions for a short duration and at low temperatures on the parent body.

Oxygen isotopic heterogeneity is observed among and within grossite-bearing FGIs in reduced CV chondrites, which can be interpreted as a result of mineralogically controlled oxygen isotopic exchange with an ^{16}O-poor fluid during metamorphism on the parent body. Grossite and perovskite underwent nearly complete oxygen isotopic exchange with the fluid and became the most ^{16}O-poor, while hibonite and spinel retained initial ^{16}O-rich compositions established during condensation in an ^{16}O-rich gas reservoir. Melilite experienced partial to complete oxygen isotopic

exchange with the fluid, recording a range of compositions extending from primordial ^{16}O-rich gas to secondary ^{16}O-poor fluid.

CRediT authorship contribution statement

Jangmi Han: Conceptualization, Investigation, Writing - Original Draft, Writing - Review & Editing, Visualization, Project administration, Funding acquisition

Kazuhide Nagashima: Investigation, Resources, Data Curation, Writing - Review & Editing, Visualization

Changkun Park: Investigation, Resources, Writing - Review & Editing

Alexander N. Krot: Investigation, Writing - Review & Editing

Lindsay P. Keller: Resources, Data Curation, Writing - Review & Editing, Supervision, Funding acquisition

ACKNOWLEDGEMENTS

This study was supported in part by NASA grants 80NSSC21K1558 (JH) and 80NSSC23K0253 (ANK), NASA ISFM funding to the JSC Coordinated Analysis Work Package (LPK), and KOPRI grant PE24050 (CP). We thank Dr. Kimura and two anonymous reviewers for constructive reviews and Dr. Kita for editorial handling. We gratefully acknowledge the access to the Electron Microprobe Lab at KOPRI, the Electron Beam Analysis Labs at NASA JSC, and the W. M. Keck Cosmochemistry Laboratory at University of Hawai‘i at Mānoa. We thank Dr. Zolensky for providing the Efremovka sample. Two TIL meteorite samples were loaned from the KOPRI Korea Curation of Antarctic Meteorites (KOREAMET) program.

APPENDIX A. SUPPLEMENTARY MATERIAL

The supplementary figures associated with this article contain SEM BSE and EDS maps of the entire view of grossite-bearing refractory inclusions studied, as well as SEM BSE images that indicate the locations of FIB sections and SIMS spots from these inclusions. In addition, additional BF STEM images and TEM EDX maps of five FIB sections analyzed for this study are provided. The supplementary tables contain a complete chemical data set obtained using EPMA and TEM EDX.

Data availability

Data are available through Mendeley Data at https://doi.org/10.17632/ystpymjrmm.2.

REFERENCES

Abreu N. M. and Brearley A. J. (2011) Deciphering the nebular and asteroidal record of silicates and organic material in the matrix of the reduced CV3 chondrite Vigarano. Meteorit. Planet. Sci. 46, 252–274.

Aléon J., Krot A. N., McKeegan K. D., MacPherson G. J. and Ulyanov A. A. (2005) Fine-grained, spinel-rich inclusions from the reduced CV chondrite Efremovka: II. Oxygen isotopic compositions. Meteorit. Planet. Sci. 40, 1043–1058.

Bak T., Nowotny J. and Sorrel C. C. (2004) Chemical diffusion in calcium titanate. J. Phys. Chem. Solids 65, 1229–1241.

Blum J. D., Wasserburg G. J., Hutcheon I. D., Beckett J. R. and Stolper E. M. (1989) Origin of opaque assemblages in C3V meteorites: Implications for nebular and planetary processes. Geochim. Cosmochim. Acta 53, 543–556.

Bonal L., Quirico E., Bourot-Denise M. and Montagnac G. (2006) Determination of the petrologic type of CV3 chondrites by Raman spectroscopy of included organic matter. Geochim. Cosmochim. Acta 70, 1849–1863.

Bonal L., Gattacceca J., Garenne A., Eschrig J., Rochette P. and Ruggiu L. K. (2020) Water and heat: New constraints on the evolution of the CV chondrite parent body. Geochim. Cosmochim. Acta 276, 363–383.

Brearley A. J. and Krot A. N. (2013) Metasomatism in the early solar system: The record from chondritic meteorites. In: Metasomatism and the Chemical Transformation of Rock. Lecture Notes in Earth System Sciences. Springer, Berlin, Heidelberg, pp. 659–789.

Che S. and Brearley A. J. (2021) An evolutionary condensation sequence revealed by mineralogically-distinct nodules in fine-grained, spinel-rich inclusions from CV3 chondrites: Implications for the genetic links between different types of non-igneous refractory inclusions. Geochim. Cosmochim. Acta 308, 75–100.

Christophe Michel-Lévy M., Kurat G. and Brandstätter (1982) A new calcium-aluminate from a refractory inclusion in the Leoville carbonaceous chondrite. Earth Planet. Sci. Lett. 61, 13–22.

Costa F. and Chakraborty S. (2008) The effect of water on Si and O diffusion rates in olivine and implications for transport properties and processes in the upper mantle. Phys. Earth Planet. Inter. 166, 11–29.

Duran A., Sirera R., Pérez-Nicolás M., Navarro-Blasco I., Fernández J. M. and Alvarez J. I. (2016) Study of the early hydration of calcium aluminates in the presence of different metallic salts. Cem. Concr. Res. 81, 1–15.

Ebel D. S. and Grossman L. (2000) Condensation in dust-enriched systems. Geochim. Cosmochim. Acta 64, 339–366.

Edmonds R. N. and Majumdar A. J. (1989) The hydration of Secar 71 aluminous cement at different temperatures. Cem. Concr. Res. 19, 289–294.

Elphick S. C., Graham C. M. and Dennis P. F. (1988) An ion microprobe study of anhydrous oxygen diffusion in anorthite: a comparison with hydrothermal data and some geological

implications. Contrib. Mineral. Petrol. 100, 490–495.
Fagan T. J., Krot A. N., Keil K. and Yurimoto H. (2004) Oxygen isotopic alteration in Ca-Al-rich inclusions from Efremovka: Nebular or parent body setting? Meteorit. Planet. Sci. 39, 1257–1272.
Fedkin A. V. and Grossman L. (2006) The fayalite content of chondritic olivine: Obstacle to understanding the condensation of rocky material. In: Meteorites and the early solar system II. Arizona University Press, Tucson, pp. 279–294.
Grossman L. (1972) Condensation in the primitive solar nebula. Geochim. Cosmochim. Acta 36, 597–619.
Grossman L. (2010) Vapor-condensed phase processes in the early solar system. Meteorit. Planet. Sci. 45, 7–20.
Grossman J. N. and Brearley A. J. (2005) The onset of metamorphism in ordinary and carbonaceous chondrites. Meteorit. Planet. Sci. 40, 87–122.
Han J. and Brearley A. J. (2017) Microstructures and formation history of melilite-rich calcium–aluminum-rich inclusions from the ALHA77307 CO3.0 chondrite. Geochim. Cosmochim. Acta 201, 136–154.
Han J., Jacobsen G., Liu M.-C., Brearley A.J., Matzel J. E. and Keller L. P. (2019) Origin of ^{16}O-rich fine-grained Ca-Al-rich inclusions of different mineralogy and texture. Geochemistry 79, 125543.
Han J., Park C. and Brearley A. J. (2022) A record of low-temperature asteroidal processes of amoeboid olivine aggregates from the Kainsaz CO3.2 chondrite. Geochim. Cosmochim. Acta 322, 109–128.
Huss G. R., Rubin A. E. and Grossman J. N. (2006) Thermal Metamorphism in Chondrites. In: Meteorites and the Early Solar System II. Arizona University Press, Tucson, pp. 567–586.
Ichimura S., Seto Y. and Tomeoka K. (2017) Nepheline formation in chondrite parent bodies: Verification through experiments. Geochim. Cosmochim. Acta 210, 114–131.
Itoh S., Kojima H. and Yurimoto H. (2004) Petrography and oxygen isotopic compositions in refractory inclusions from CO chondrites. Geochim. Cosmochim. Acta 68, 183–194.
Ivanova M. A., Petaev M. I., MacPherson G. J., Nazarov M. A., Taylor L. A. and Wood J. A. (2002) The first known natural occurrence of calcium monoaluminate, in a calcium-aluminum-rich inclusion from the CH chondrite Northwest Africa 470. Meteorit. Planet. Sci. 37, 1337–1344.
Jogo K., Nakamura T., Noguchi T. And Zolotov M. Y. (2009) Fayalite in the Vigarano CV3 carbonaceous chondrite: Occurrences, formation age and conditions. Earth Planet. Sci. Lett. 287, 320–328.
Johnson C. A. and Prinz M. (1991) Chromite and olivine in type II chondrules in carbonaceous and ordinary chondrites: Implications for thermal histories and group differences. Geochim. Cosmochim. Acta 55, 893–904.
Kimura M., El Goresy A., Palme H. and Zinner E. (1993) Ca-, Al-rich inclusions in the unique

chondrite ALH85085: Petrology, chemistry, and isotopic compositions. Geochim. Cosmochim. Acta 57, 2329–2359.

Kimura M., Nakajima H., Hiyagon H. and Weisberg M. K. (2006) Spinel group minerals in LL3.00–6 chondrites: Indicators of nebular and parent body processes. Geochim. Cosmochim. Acta 70, 5634–5650.

Klaus S. R., Neubauer J. and Goetz-Neunhoeffer F. (2013) Hydration kinetics of CA2 and CA – Investigations performed on a synthetic calcium aluminate cement. Cem. Concr. Res. 43, 62–69.

Kornacki A. S. and Wood J. A. (1985) Mineral chemistry and origin of spinel-rich inclusions in the Allende CV3 chondrite. Geochim. Cosmochim. Acta 49, 1219–1237.

Krot A. N., MacPherson G. J., Ulyanov A. A. and Petaev M. I. (2004) Fine-grained, spinel-rich inclusions from the reduced CV chondrites Efremovka and Leoville: I. Mineralogy, petrology, and bulk chemistry. Meteorit. Planet. Sci. 39, 1517–1553.

Krot A. N., Nagashima K., Simon S. B., Ma C., Connolly Jr H. C., Huss G. R., Davis A. M. and Bizzarro M. (2019a) Mineralogy, petrography, and oxygen and aluminum-magnesium isotope systematics of grossite-bearing refractory inclusions. Geochemistry 79, 125529.

Krot A. N., Nagashima K., Fintor K. and Pál-Molnár E. (2019b) Evidence for oxygen-isotope exchange in refractory inclusions from Kaba (CV3.1) carbonaceous chondrite during fluid-rock interaction on the CV parent asteroid. Geochim. Cosmochim. Acta 246, 419–435.

Krot A. N., Petaev M. I. and Nagashima K. (2021) Infiltration metasomatism of the Allende coarse-grained calcium-aluminum-rich inclusions. Prog. Earth Planet. Sci. 8, 61.

Krot A. N., Nagashima K., MacPherson G. J. and Ulyanov A. A. (2022) On the nature of oxygen-isotope heterogeneity of igneous calcium-aluminum-rich inclusions in CV carbonaceous chondrites. Geochim. Cosmochim. Acta 332, 327–354.

Lee M. R., Hutchison R. and Graham A. (1996) Aqueous alteration in the matrix of the Vigarano (CV3) carbonaceous chondrite. Meteorit. Planet. Sci. 31, 477–483.

Liermann H.-P. and Ganguly J. (2002) Diffusion kinetics of Fe^{2+} and Mg in aluminous spinel: Experimental determination and applications. Geochim. Cosmochim. Acta 66, 2903–2913.

Lodders K. (2003) Solar system abundances and condensation temperatures of the elements. Astrophys. J. 591, 1220–1247.

Ma C., Kampf A. R., Connolly Jr. H. C., Beckett J. R., Rossman G. R., Sweeney Smith S. A. and Schrader D. L. (2011) Krotite, $CaAl_2O_4$, a new refractory mineral from the NWA 1934 meteorite. Am. Mineral. 96, 709–715.

MacPherson G. J. and Krot A. N. (2014) The formation of Ca-, Fe-rich silicates in reduced and oxidized CV chondrites: The roles of impact-modified porosity and permeability, and heterogeneous distribution of water ices. Meteorit. Planet. Sci. 49, 1250–1270.

MacPherson G. J., Krot A. N. and Nagashima K. (2020) Al-Mg isotopic study of spinel-rich fine-grained CAIs. Meteorit. Planet. Sci. 55, 2519–2538.

Makide K., Nagashima K., Krot A. N., Huss G. R., Hutcheon I. D. and Bischoff A. (2009) Oxygen- and magnesium-isotope compositions of calcium-aluminum-rich inclusions from CR2 carbonaceous chondrites. Geochim. Cosmochim. Acta 73, 5018–5051.

Maruyama S. and Tomioka N. (2011) Ca-Al-Fe-rich inclusion in the Vigarano CV3 chondrite. Meteorit. Planet. Sci. 46, 690–700.

Matusinović T. and Vrbos N. (1993) Alkali metal salts as set accelerators for high alumina cement. Cem. Concr. Res. 23, 177–186.

McKeegan K. D., Kallio A. P. A., Heber V. S., Jarzebinski G., Mao P. H., Coath C. D., Kunihiro T., Wiens R. C., Nordholt J. E., Moses R. W. Jr., Reisenfeld D. B., Jurewicz A. J. G. and Burnett D. S. (2011) The oxygen isotopic composition of the Sun inferred from captured solar wind. Science 332, 1528–1532.

Nagashima K., Krot A. N. and Huss G. R. (2015) Oxygen-isotope compositions of chondrule silicates and matrix grains in Kakangari K-grouplet chondrite. Geochim. Cosmochim. Acta 151, 49–67.

Nakashima D., Ushikubo T., Joswiak D. J., Brownlee D. E., Matrajt G., Weisberg M. K., Zolensky M. E. and Kita N. T. (2012) Oxygen isotopes in crystalline silicates of comet Wild 2: A comparison of oxygen isotope systematics between Wild 2 particles and chondritic materials. Earth Planet. Sci. Lett. 357–358, 355–365.

Nomura K. and Miyamoto M. (1998) Hydrothermal experiments on alteration of Ca–Al-rich inclusions (CAIs) in carbonaceous chondrites: Implication for aqueous alteration in parent asteroids. Geochim. Cosmochim. Acta 62, 3575–3588.

Petaev M. I. and Wood J. A. (1998) The condensation with partial isolation (CWPI) model of condensation in the solar nebula. Meteorit. Planet. Sci. 33, 1123–1137.

Petaev M. I. and Wood J. A. (2005) Meteoritic constraints on temperatures, pressures, cooling rates, chemical compositions, and modes of condensation in the solar nebula. In: Chondrites and the protoplanetary disk ASP Conference Series 341. San Francisco, California: Astronomical Society of the Pacific. pp. 373–406.

Pöllmann H. (2012) Calcium aluminate cements – Raw materials, differences, hydration and properties. Reviews in Mineralogy & Geochemistry Vol.74, pp. 1–82.

Pouchou J. L. and Pichoir F. (1984) A new model for quantitative x-ray microanalysis. Part I: application to the analysis of homogeneous samples. La Recherche Aerospatiale 3, 13–38.

Putnis A. (2009) Mineral replacement reactions. In: Thermodynamics and Kinetics of Water-Rock Interaction. Reviews in Mineralogy and Geochemistry Vol. 70, pp. 87–124.

Robens E., Rauschen R., Kaub J., Parras J. P., Kemp D., Freeman C. L. and De Souza R. A. (2022) Perovskite crystal symmetry and oxygen-ion transport: a molecular-dynamics study of perovskite. J. Mater. Chem. A 10, 2388–2397.

Ryerson F. J. and McKeegan K. D. (1994) Determination of oxygen self-diffusion in åkermanite, anorthite, diopside, and spinel: Implications for oxygen isotopic anomalies and the thermal histories of Ca-Al-rich inclusions. Geochim. Cosmochim. Acta 58, 3713–3734.

Schmitt N., Hernandez J.-F, Lamour V., Berthaud Y., Meunier P. and Poirier J. (2000) Coupling between kinetics of dehydration, physical and mechanical behaviour for high alumina castable. Cem. Concr. Res. 30, 1597–1607.

Simon S. B., Krot A. N., Nagashima K., Kööp L. and Davis A. M. (2019a) Condensate refractory inclusions from the CO3.00 chondrite Dominion Range 08006: petrography, mineral chemistry, and isotopic compositions. Geochim. Cosmochim. Acta 246, 109–122.

Simon S. B., Krot A. N. and Nagashima K. (2019b) Oxygen and Al-Mg isotopic compositions of grossite-bearing refractory inclusions from CO3 chondrites. Meteorit. Planet. Sci. 54, 1362–1378.

Ukrainczyk N. (2010) Kinetic modeling of calcium aluminate cement hydration. Chem. Eng. Sci. 65, 5605–5614.

Ukrainczyk N., Matusinovic T., Kurajica S., Zimmermann B. and Sipusic J. (2007) Dehydration of a layered double hydroxide – C_2AH_8. Thermochim. Acta 464, 7–15.

Wasson J. T., Yurimoto H. and Russell S. S. (2001) ^{16}O-rich melilite in CO3.0 chondrites: Possible formation of common, ^{16}O-poor melilite by aqueous alteration. Geochim. Cosmochim. Acta 65, 4539–4549.

Weber D. and Bischoff A. (1994) The occurrence of grossite ($CaAl_2O_4$) in chondrites. Geochim. Cosmochim. Acta 58, 3855–3877.

Wood J. A. and Hashimoto A. (1993) Mineral equilibrium in fractionated nebular systems. Geochim. Cosmochim. Acta 57, 2377–2388.

Yoneda S. and Grossman L. (1995) Condensation of $CaO–MgO–Al_2O_3–SiO_2$ liquids from cosmic gases. Geochim. Cosmochim. Acta 59, 3413–3444.

Yurimoto H., Morioka M. and Nagasawa H. (1989) Diffusion in single crystals of melilite: I. Oxygen. Geochim. Cosmochim. Acta 53, 2387–2394.

Zhang M., Bonato E., King A. J., Russell S. S., Tang G. and Lin Y. (2020) Petrology and oxygen isotopic compositions of calcium-aluminum-rich inclusions in primitive CO3.0-3.1 chondrites. Meteorit. Planet. Sci. 55, 911–935.

Zolotov M. Y. (2012) Aqueous fluid composition in CI chondritic materials: Chemical equilibrium assessments in closed systems. Icarus 220, 713–729.

Zolotov M. Y., Mironenko M. V. and Shock E. L. (2006) Thermodynamic constraints on fayalite formation on parent bodies of chondrites. Meteorit. Planet. Sci. 41, 1775–1796.

TABLES

Table 1. Oxygen isotopic compositions of individual minerals in grossite-bearing FGIs from reduced CV chondrites.

CAI #	mineral	spot #	$\delta^{18}O$	2σ	$\delta^{17}O$	2σ	$\Delta^{17}O$	2σ
E-B-1	hib	h1	−44.9	0.9	−48.2	2.3	−24.8	2.3
	hib	h2	−46.2	0.9	−45.3	2.1	−21.3	2.1
	hib	h3	−45.7	0.9	−47.3	2.3	−23.6	2.3
	hib	h4	−45.2	1.1	−47.2	2.2	−23.7	2.3
	sp	s1	−46.1	1.2	−48.9	3.0	−25.0	3.2
	sp	s2	−46.5	1.3	−46.5	2.4	−22.4	2.6
	mel	m1	5.4	1.0	0.8	2.3	−2.0	2.3
	mel	m2	−0.5	1.5	−6.3	2.4	−6.0	2.4
	mel	m3	8.1	1.1	1.8	2.5	−2.4	2.4
	mel	m4	8.1	1.1	1.8	2.2	−2.4	2.2
	mel	m5	5.8	1.6	−0.3	2.0	−3.3	2.1
	mel	m6	8.7	0.9	1.6	2.5	−2.9	2.4
	gro	g1	4.8	0.9	−1.8	2.5	−4.3	2.5
	gro	g2	6.9	1.0	0.3	2.3	−3.3	2.4
	gro	g3	5.8	1.0	−2.0	2.3	−5.1	2.3
	gro	g4	5.3	1.2	−0.5	2.2	−3.2	2.2
	gro	g5	5.6	0.9	0.5	2.3	−2.4	2.3
	gro	g6	5.7	1.0	−0.5	2.5	−3.4	2.5
TIL 3-11	hib	h1	−47.0	1.2	−47.7	2.4	−23.2	2.5
	sp	s1	−46.1	1.3	−49.4	2.4	−25.5	2.6
	mel	m1	3.5	1.2	−2.9	2.7	−4.7	2.7
	mel	m2	2.6	1.5	−3.3	2.4	−4.6	2.4
	gro	g1	7.6	1.3	−0.1	2.0	−4.0	2.0
	gro	g2	9.4	1.2	1.1	2.4	−3.8	2.4
	gro	g3	10.1	1.3	3.7	2.4	−1.6	2.4
	gro	g4	9.1	1.1	2.1	2.1	−2.7	2.1
	gro	g5	3.3	1.9	−3.9	2.4	−5.6	2.5
	gro	g6	9.7	1.3	2.0	2.0	−3.1	2.0
TIL 3-16	sp	s1	−45.8	1.2	−48.3	2.3	−24.4	2.5
	sp	s2	−45.9	1.2	−48.8	2.4	−25.0	2.6
	mel	m1	−29.4	1.2	−32.0	2.2	−16.7	2.2
	mel	m2	−37.3	1.0	−37.9	2.2	−18.5	2.2
	mel	m3	−25.8	3.3	−26.1	4.4	−12.7	4.6
	gro	g1	6.4	1.3	−0.7	2.3	−4.0	2.4
	gro	g2	8.4	1.3	1.6	2.1	−2.8	2.1
	gro	g3	6.9	1.5	−0.7	2.2	−4.3	2.3
TIL 7-18	sp	s1	−45.6	1.3	−47.2	2.4	−23.5	2.6
	sp	s2	−43.5	1.3	−44.9	2.5	−22.3	2.7
	mel	m1	−9.3	3.1	−13.6	2.6	−8.8	3.0
	gro	g1	3.2	1.2	−3.2	2.5	−4.9	2.5
	gro	g2	7.2	1.0	−0.4	2.1	−4.1	2.1

	gro	g3	6.3	1.0	−2.4	2.5	−5.7	2.5
	gro	g4	5.5	1.5	−2.2	2.2	−5.0	2.3
TIL 7-05	sp	s1	−45.9	1.3	−48.2	2.7	−24.3	2.9
	sp	s2	−45.8	1.3	−46.0	2.4	−22.2	2.7
	sp	s3	−46.3	1.2	−47.0	2.3	−22.9	2.5
	mel	m1	8.9	1.5	2.5	2.1	−2.1	2.1
	mel	m2	8.0	1.5	−0.2	2.8	−4.3	2.8
	mel	m3	−20.0	1.0	−24.5	2.1	−14.1	2.1
	mel	m4	−4.9	1.3	−10.9	2.3	−8.4	2.3
	mel	m5	−1.0	1.1	−7.1	2.6	−6.6	2.5
	mel	m6	−46.2	1.1	−46.9	2.2	−22.9	2.2
	gro	g1	11.0	1.1	2.3	2.4	−3.4	2.4
	gro	g2	10.3	0.8	4.0	2.4	−1.4	2.4
	gro	g3	11.1	1.0	3.3	2.1	−2.4	2.1
	gro	g4	11.9	1.0	4.0	2.1	−2.2	2.1
	gro	g5	10.6	1.1	3.9	2.6	−1.6	2.6
	gro	g6	11.3	1.0	3.3	2.4	−2.5	2.4
	gro	g7	10.1	1.2	1.8	2.4	−3.4	2.4
	gro	g8	10.2	1.0	3.1	2.1	−2.2	2.2
	pv	p1	−1.2	1.4	−3.4	1.8	−2.8	1.9
	pv	p2	−1.4	2.8	−3.9	2.5	−3.2	2.9
	pv	p3	−1.1	1.4	−3.1	1.9	−2.5	2.1
	pv	p4	−0.9	1.5	−2.1	1.8	−1.6	1.9
	pv	p5	2.8	1.3	−0.2	1.6	−1.7	1.8
	pv	p6	−0.8	1.4	−3.0	1.7	−2.6	1.8
	pv	p7	−0.8	1.5	−2.9	1.7	−2.4	1.9
TIL 7-08	hib	h1	−43.2	1.0	−45.2	2.2	−22.8	2.2
	sp	s1	−46.2	1.3	−47.7	2.4	−23.7	2.6
	sp	s2	−45.7	1.2	−47.6	2.3	−23.8	2.5
	sp	s3	−46.4	1.3	−47.8	2.3	−23.7	2.6
	mel	m1	−46.4	1.1	−49.2	2.5	−25.1	2.5
	mel	m2	−38.7	1.2	−41.4	2.6	−21.3	2.6
	mel	m3	−35.1	1.2	−38.3	2.2	−20.1	2.2
	mel	m4	−16.1	1.2	−20.9	2.4	−12.5	2.4
	mel	m5	−17.5	1.1	−21.3	2.2	−12.3	2.2
	mel	m6	−27.4	1.5	−28.9	2.4	−14.7	2.5
	gro	g1	−10.3	0.9	−15.3	2.6	−9.9	2.6
	gro	g2	−4.1	1.0	−10.6	2.7	−8.5	2.7
	gro	g3	−16.9	1.0	−20.4	2.6	−11.6	2.6
	gro	g4	−6.2	1.0	−12.1	2.4	−8.9	2.4
	pv	p1	2.9	1.5	0.2	1.7	−1.3	1.8
	pv	p2	−0.1	1.2	−2.2	1.8	−2.1	1.9
	pv	p3	3.2	1.3	−0.1	1.8	−1.8	1.9
	pv	p4	−3.0	1.5	−4.0	1.8	−2.4	2.0
	pv	p5	0.0	1.3	−2.5	1.7	−2.5	1.8
	pv	p6	2.8	1.3	−0.7	1.9	−2.1	2.0

FIGURES

Figure 1. (a, d-e) BSE images, (b) combined x-ray map in Mg (red), Ca (green), Al (blue), and Ti (yellow), and (c) elemental Fe x-ray map of the CAI *E-B-1*. The x-ray maps shown in (b-c) were taken from a region shown in (a). This inclusion is dominated by numerous hibonite-spinel-rich nodules. Grossite-rich nodules are rare and occur only in the CAI periphery. Hercynite occurs as a thick layer surrounding grossite. Abbreviations hereafter: an = anorthite; di = diopside; gro = grossite; hc = hercynite; hib = hibonite; mel = melilite; pv = perovskite; sp = spinel.

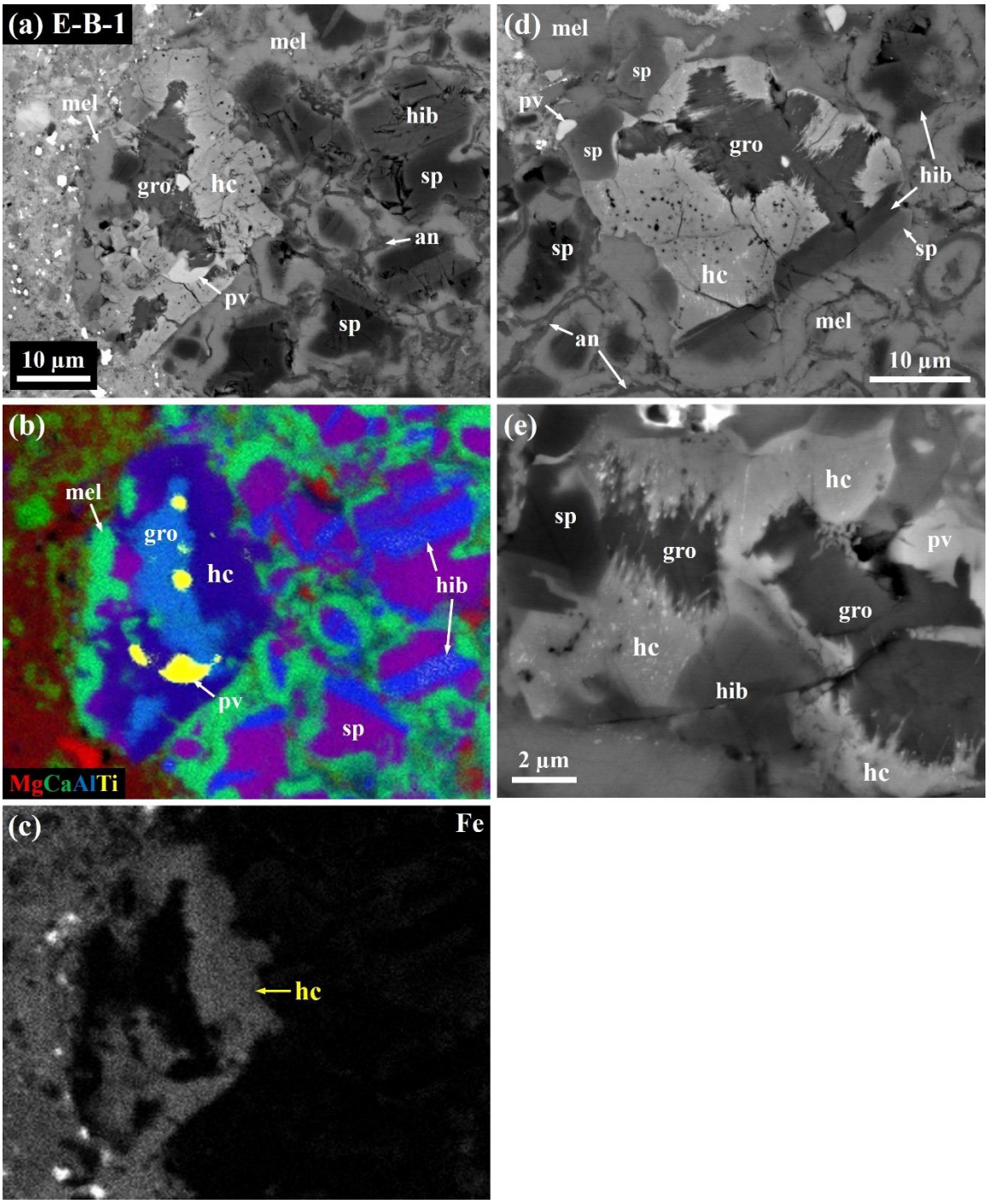

Figure 2. BSE images of three CAIs *TIL 3-11*, *TIL 3-16*, and *TIL 7-18*. Regions outlined in (a-c) are shown in detail in (d-f), respectively. These CAIs consist of spinel-rich nodules. The cores of some nodules contain grossite surrounded by hercynite, ±hibonite, spinel, melilite, and diopside. Hercynite contains numerous, aligned pores and shares sharp grain boundaries with adjacent spinel, hibonite, and melilite. A SIMS pit in (f) is indicated by a yellow arrow.

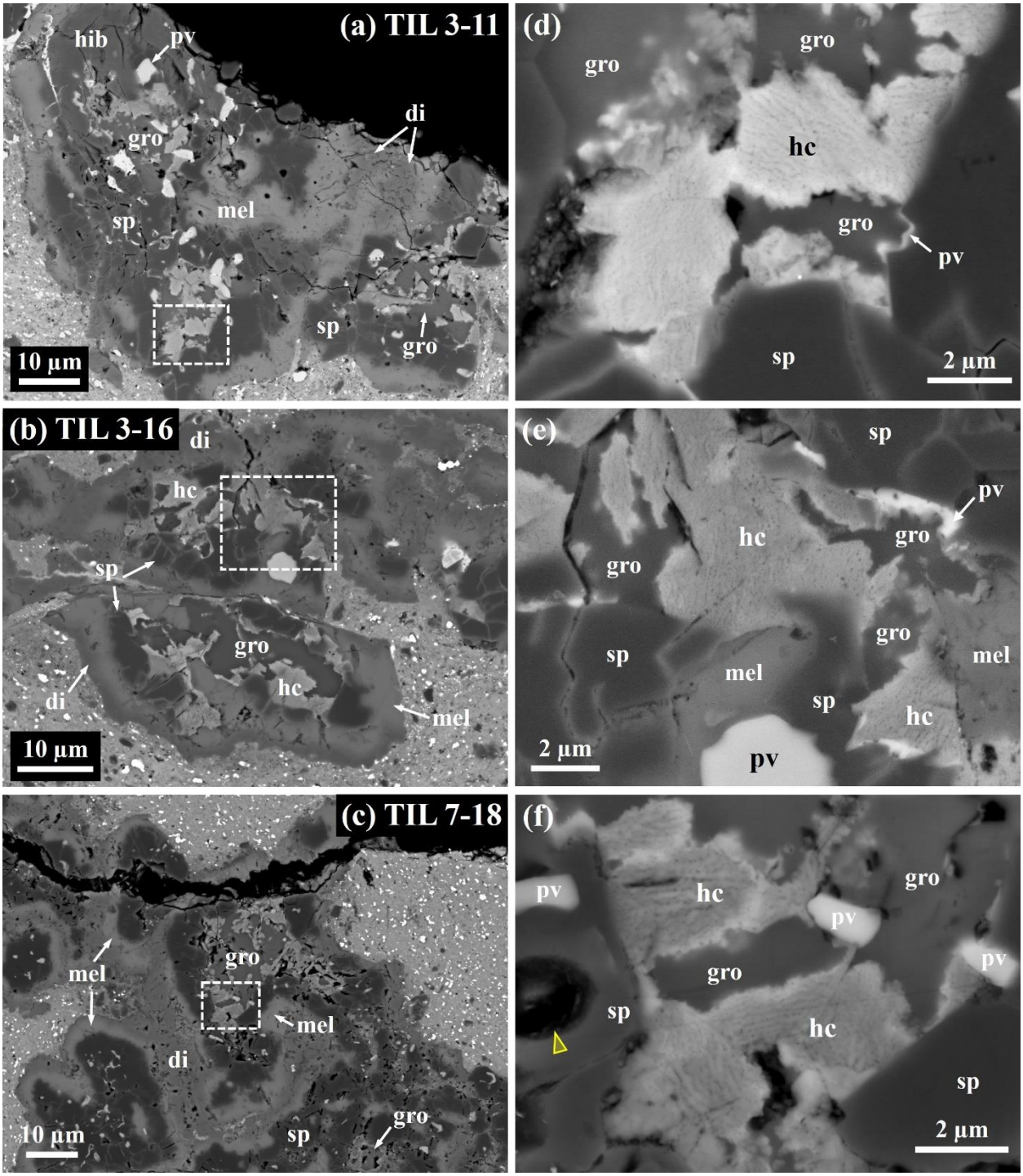

Figure 3. BSE images of the CAI *TIL 7-05*. A region outlined in (a) is shown in detail in (c). Grossite occurs in a core surrounded by spinel associated with perovskite. Hercynite veins occur between grossite grains and along the grossite-spinel grain boundaries. Parallel lamellae of unknown phase, indicated by large red arrows in (b, c), appear as a slightly bright contrast in some areas of grossite. SIMS pits in (c) are indicated by yellow arrows.

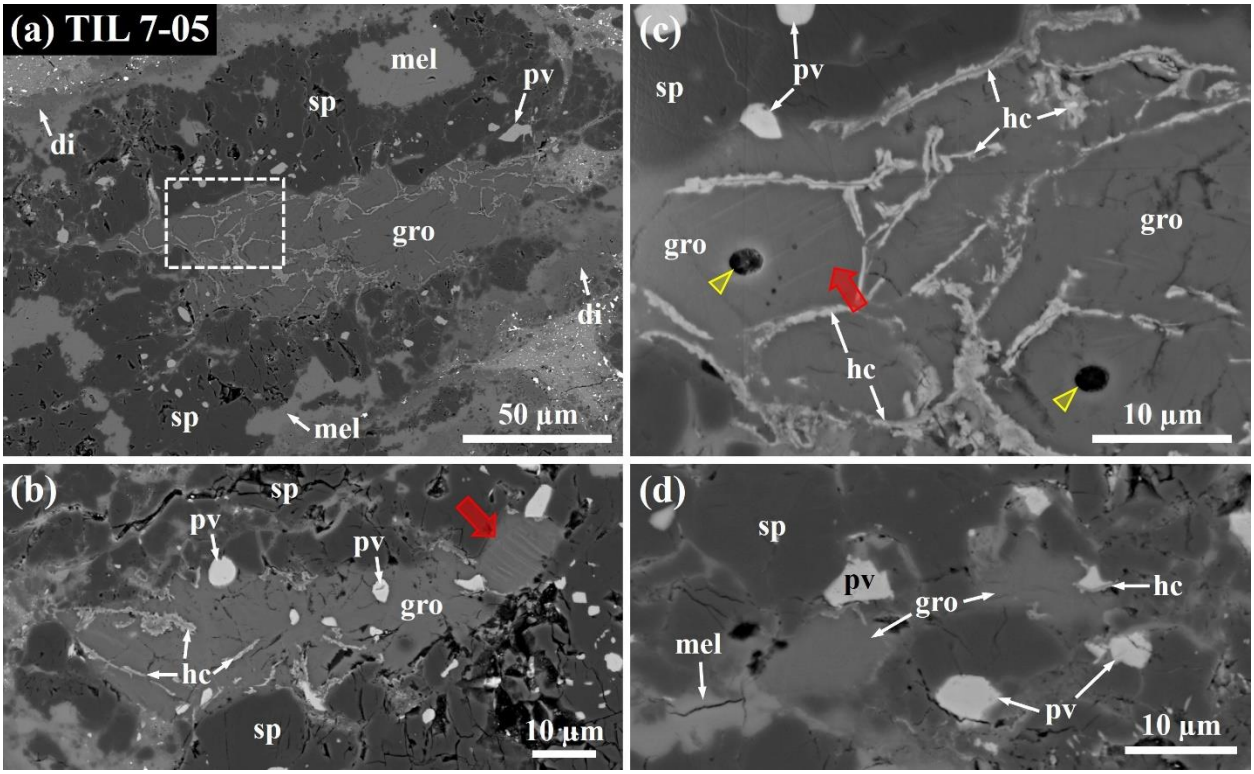

Figure 4. BSE images of the CAI *TIL 7-08*. A region outlined in (a) is shown in detail in (c). SIMS pits are indicated by yellow arrows in (d, f). This CAI is a mineralogically zoned inclusion consisting of a melilite-rich core and a spinel-rich mantle. Grossite occurs only in the melilite-rich core, with perovskite and rarely with spinel. No Fe-rich phase is observed.

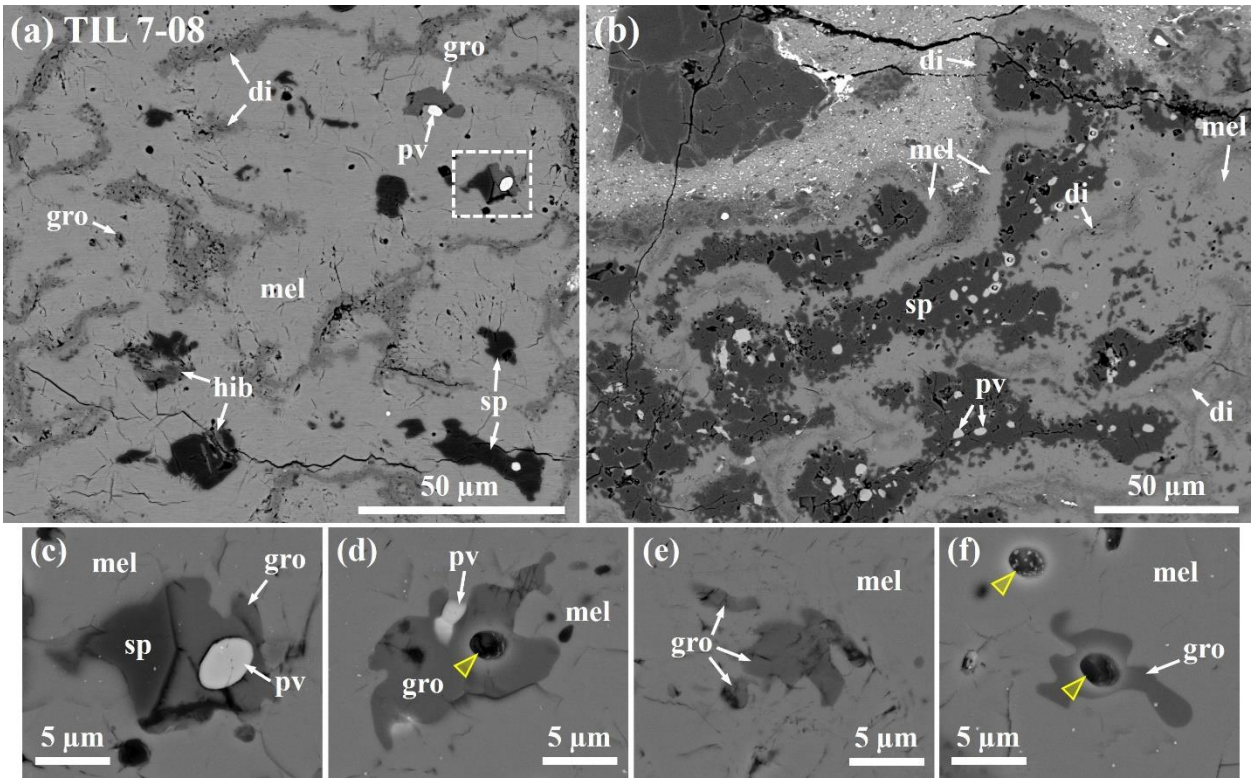

Figure 5. Variations in FeO contents of grossite and spinel among grossite-bearing FGIs from reduced CV chondrites, obtained using electron microprobe. (a) Histograms of FeO contents (wt%) in grossite. (b) A plot of Cr_2O_3 versus FeO contents (wt%) in spinel. Note a relatively wider spacing for a range of FeO contents up to 2 wt% along the x axis. Individual inclusions define somewhat distinct ranges of FeO contents in these two phases. The detection limits for Cr_2O_3 and FeO were 0.02 wt%. Abbreviations hereafter: gro-n = grossite-rich nodules; hib-sp-n = hibonite-spinel-rich nodules.

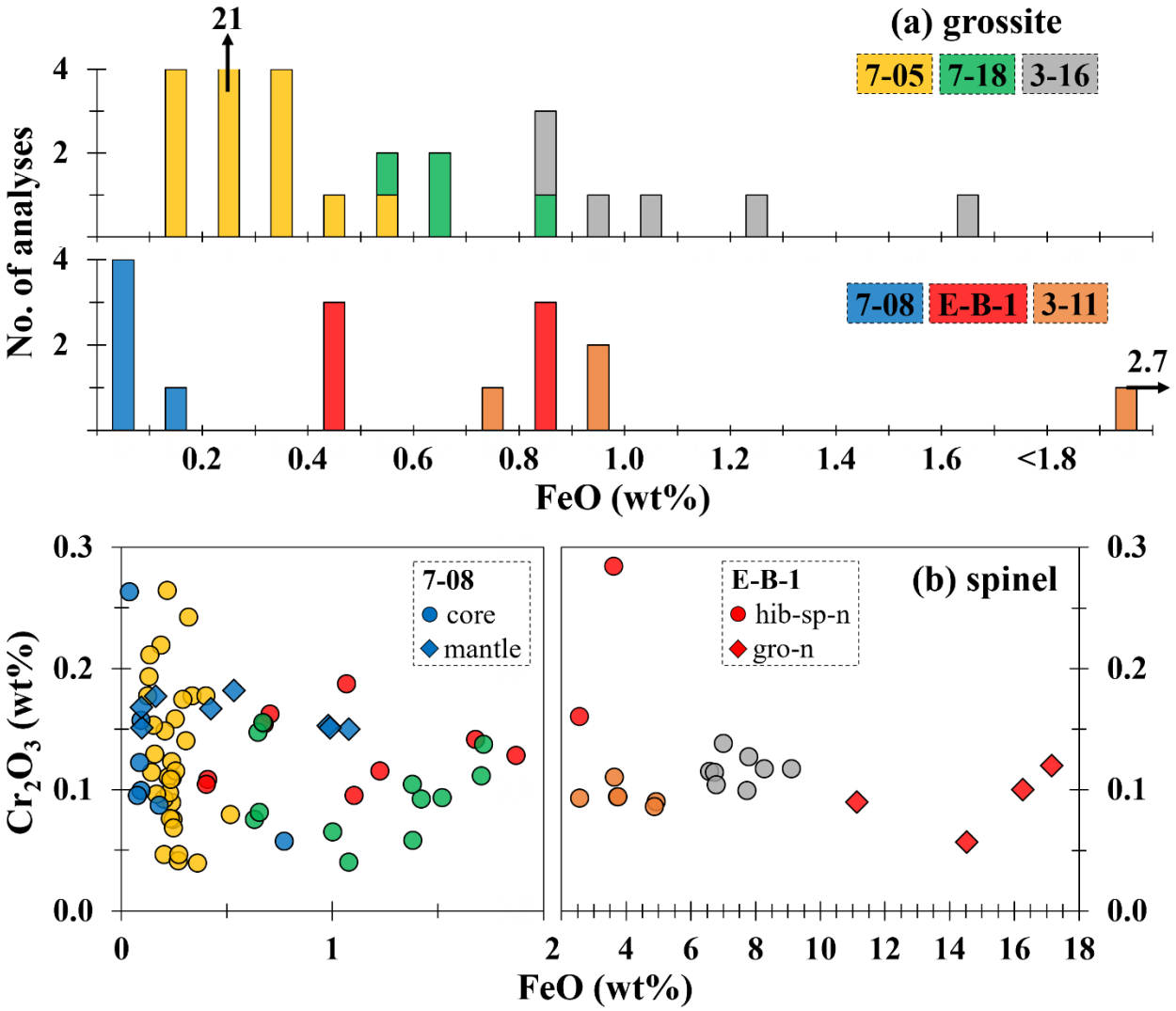

Figure 6. TEM images of the CAI *E-B-1*. (a) BF STEM image of an aggregate of oriented hercynite laths protruding into grossite. Abundant Al-rich amorphous lamellae are alternating with grossite. A region outlined in (a) is shown in detail in (b). (b) BF STEM image and combined x-ray map in Mg (red), Ca (green), and Fe (blue) showing magnetite nanoparticles at the tips of hercynite laths. (c) HRTEM image of magnetite at the tip of the hercynite lath, shown in (b). An inset is FFT pattern extracted from magnetite and grossite, which is indexed as the [111] zone axis of magnetite being parallel to the [$\bar{3}$01] zone axis of grossite. The reflections from magnetite are indicated by yellow circles, whereas the other reflections are generated from grossite. (d) BF STEM image of a faceted hercynite crystal, with radiated hercynite laths (bottom center), in contact with grossite. An inset electron diffraction pattern is indexed as the [011] zone axis of the hercynite crystal, with its faces oriented along the {111} planes. Numerous pores are associated with the amorphous lamellae. (e) BF STEM image of a rare hercynite inclusion and parallel cracks and amorphous lamellae in grossite. An inset electron diffraction pattern is indexed as the [013] zone axis of the host grossite. Abbreviations hereafter: am = Al-rich amorphous material; mgt = magnetite; p = pore.

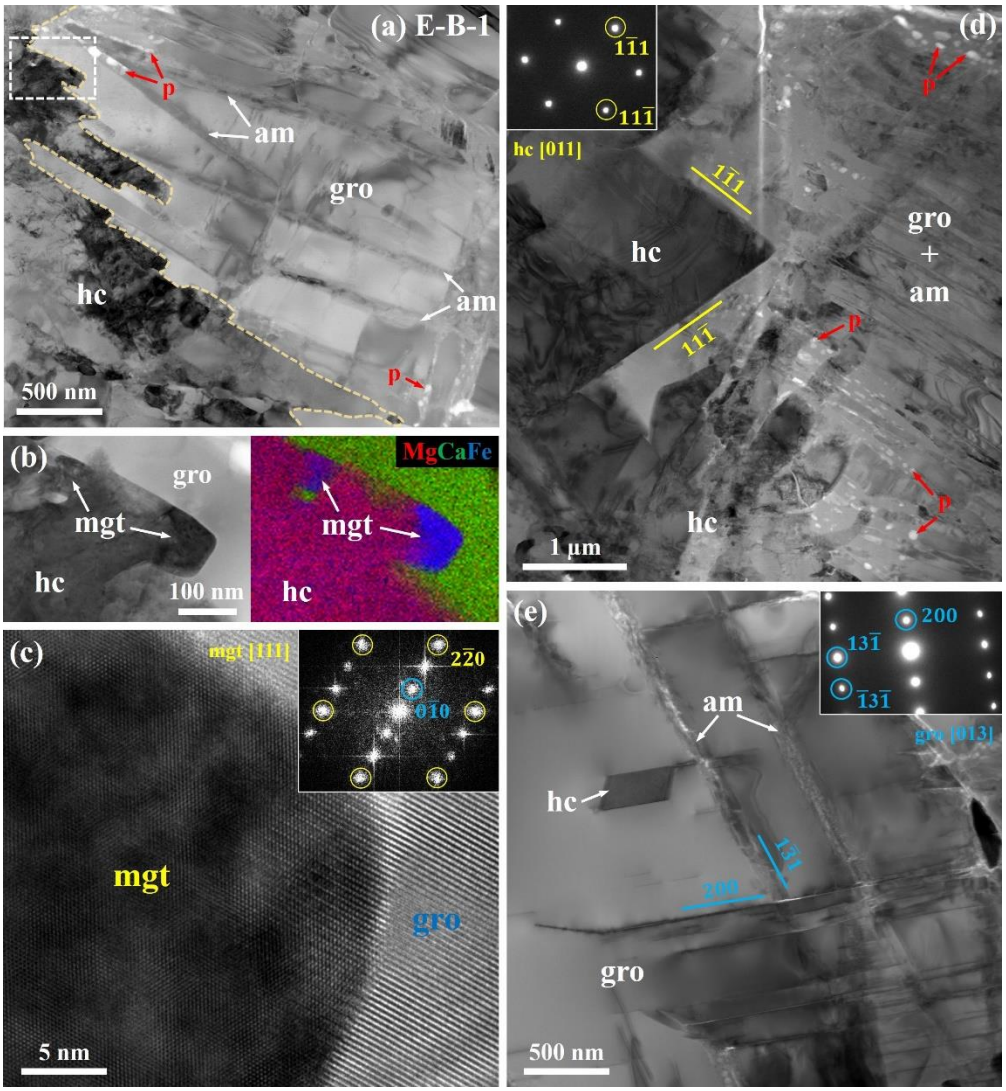

Figure 7. TEM images of the CAI *TIL 7-18*. (a-c) BF STEM images and combined x-ray map in Mg (red), Ca (green), and Fe (blue), and elemental Zn x-ray map of grossite and perovskite associated with two types of hercynite. Zinc is concentrated only in hercynite. Pores are common along individual grossite-grossite and grossite-hercynite grain boundaries. (d) BF STEM image showing a polygonal pore and magnetite nanoparticles at the interface between hercynite and grossite. Hercynite laths in contact with grossite are elongated normal to the b direction of grossite. An inset electron diffraction pattern is indexed as the [100] zone axis of grossite. (e) HRTEM image of a hercynite lath in crystallographic continuity with grossite, looking down the [100] zone axis of grossite. An inset is FFT pattern indexed as the [233] zone axis of hercynite.

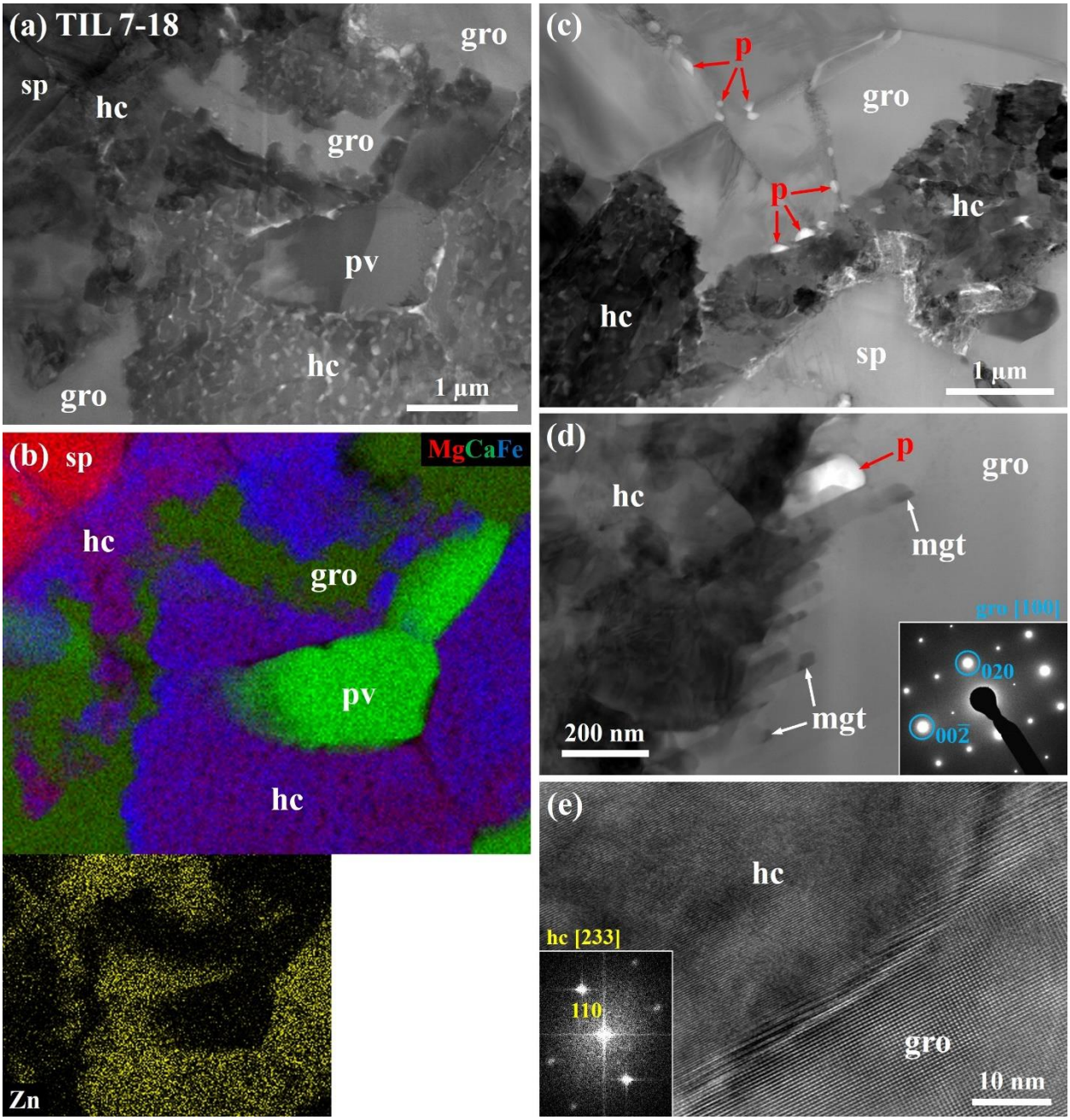

Figure 8. TEM images of the CAI *TIL 7-18*. (a, b) BF STEM images of porous hercynite crystals. Pores in these hercynite crystals are aligned and interconnected. Some edges of perovskite grains in contact with porous hercynite crystals are also porous. (c) HRTEM image of a porous hercynite crystal and its electron diffraction pattern, indexed as the [011] zone axis. Pores are faceted along the {111} plane of the host hercynite. (d) BF STEM image and combined x-ray map in S (red), Ca (green), and Fe (blue) of the outer region of a porous hercynite crystal. The occurrence of FeS-rich nanoparticles, possibly troilite, are indicated.

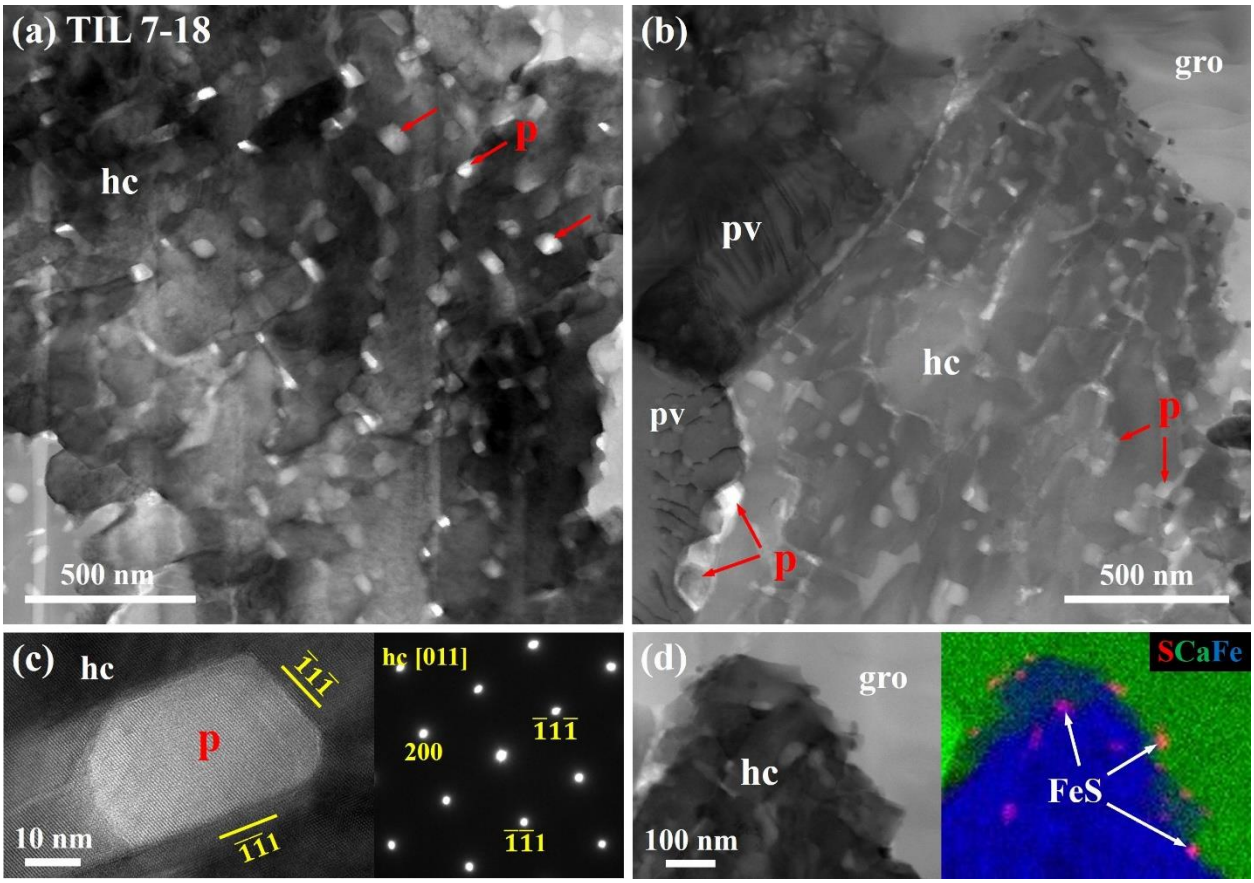

Figure 9. TEM images of the CAI *TIL 7-05*. (a) BF STEM image, combined x-ray map in Mg (red), Ca (green), and Fe (blue), and elemental Zn x-ray map of grossite grains separated by hercynite veins. These veins consist of porous aggregates of blocky to elongate hercynite grains with numerous hercynite nanocrystals. (b) HRTEM image of an Al-rich amorphous layer within grossite. Insets are BF STEM image of dark amorphous lamellae (indicated by arrows) within grossite and electron diffraction pattern indexed as the [$\bar{1}\bar{1}2$] zone axis of the host grossite.

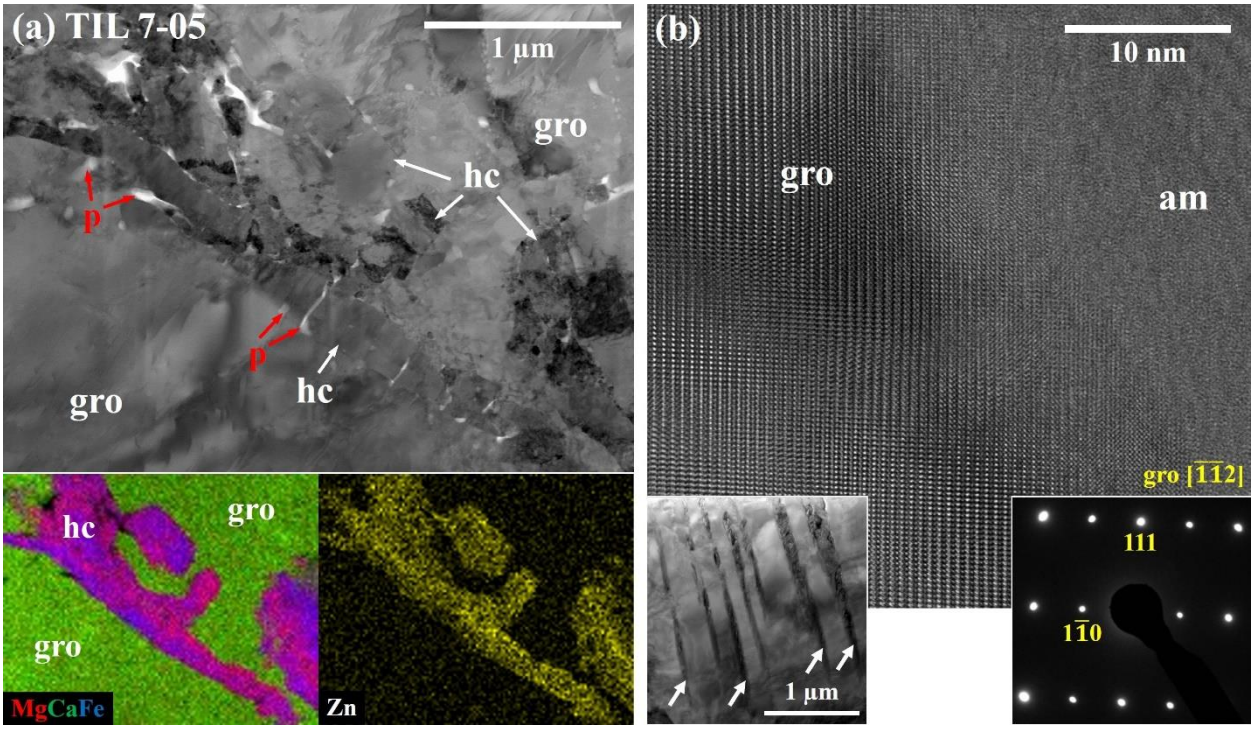

Figure 10. TEM images of the CAI *TIL 7-08*. (a) BF STEM image of grossite embayed by Al-rich amorphous material and fine-grained, porous aggregate of hercynite. Arrows indicate the occurrence of the amorphous material extending into grossite. A region outlined in (a) is shown in detail in (b). (b) BF STEM image of the interface between grossite and the hercynite aggregate.

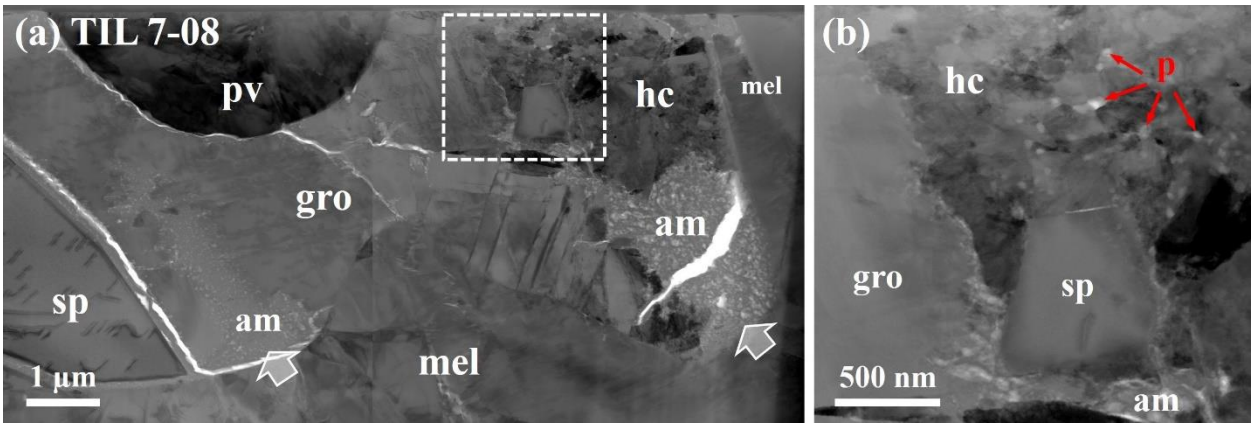

Figure 11. Comparison of hercynite compositions among four grossite-bearing FGIs from reduced CV chondrites, obtained using TEM EDX. This diagram of atomic Fe versus Zn numbers per formula unit (pfu) reveals that each inclusion exhibits variable, but somewhat different ranges. Total Fe was calculated as Fe^{2+}.

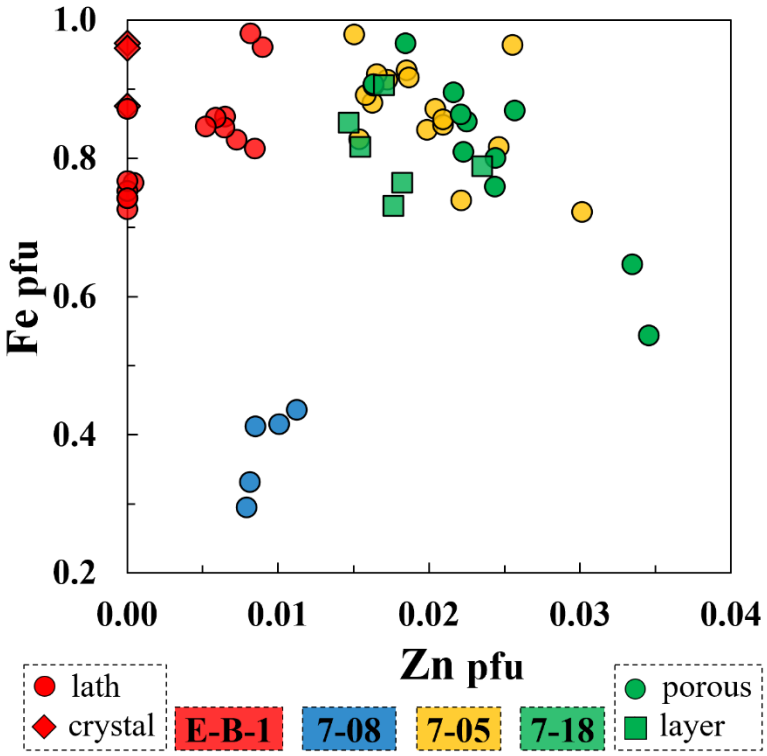

Figure 12. (a, b) BF STEM images, combined x-ray maps in Mg (red), Ca (green), and Fe (blue), and elemental Fe and Zn x-ray maps of the spinel-spinel and spinel-hercynite grain boundaries in the CAI *TIL 7-18*. The boundaries between spinel and hercynite are indicated by a dotted line in (b). (c) Distribution of FeO (red diamonds) and ZnO (yellow circles) contents along the spinel-spinel grain boundary, obtained by TEM EDX. The profiles were extracted from the solid line in (a), and G.B. represents the grain boundary between spinel grains. Progressive Fe and Zn enrichments are observed from the edges of spinel grains.

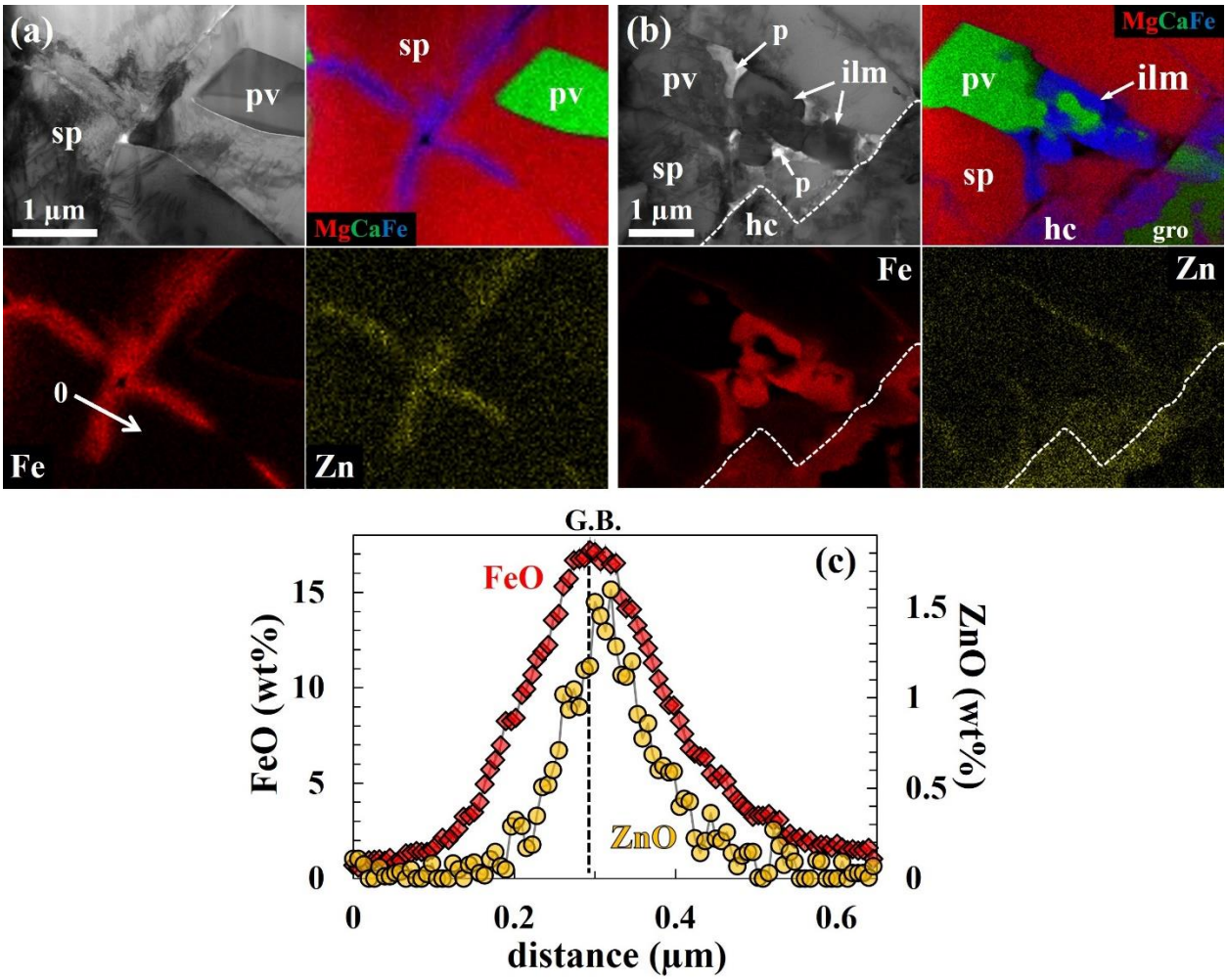

Figure 13. Oxygen isotopic compositions of individual minerals in grossite-bearing FGIs from reduced CV chondrites. The data are plotted on an oxygen three-isotope diagram ($\delta^{17}O$ vs. $\delta^{18}O$) in (a) and as deviations from the terrestrial fractionation line ($\Delta^{17}O$) in (b). The terrestrial fractionation (TF) and carbonaceous chondrite anhydrous mineral (CCAM) lines are shown for reference. The parent-body fluid composition inferred from secondary fayalite and magnetite in Kaba (CV3.1) is shown as the mass-dependent fractionation line with $\Delta^{17}O = -1.5\pm1‰$ (Krot et al., 2019b). Genesis solar wind (SW) value of $\Delta^{17}O = -28.4\pm1.8‰$ (McKeegan et al., 2011) is also indicated.